AOD data fusion with Geostationary Korea Multi-Purpose Satellite (GEO-KOMPSAT-2) instruments GEMS, AMI, and GOCI-II: Statistical and deep neural network methods

Minseok Kim[1], Jhooon Kim[1], Hyunkwang Lim[2], Seoyoung Lee[3,4], Yeseul Cho[1], Yun-Gon Lee[5], Sujung Go[3,4], Kyunghwa Lee[6]

[1]Department of Atmospheric Sciences, Yonsei University, Seoul, 03722, South Korea
[2]National Institute for Environmental Studies (NIES), Tsukuba, 305-0053, Japan
[3]Goddard Earth Sciences Technology and Research (GESTAR) II, University of Maryland Baltimore County, Baltimore, 21250, MD, USA
[4]NASA Goddard Space Flight Center (GSFC), Greenbelt, 20771, MD, USA
[5]Department of Atmospheric Sciences, Chungnam National University, Daejeon, 34134, South Korea
[6]National Institute of Environmental Research (NIER), Incheon, postal 22689, South Korea

Correspondence to: Jhoon Kim (jkim2@yonsei.ac.kr)

Abstract. Data fusion of aerosol optical depth (AOD) datasets from the second generation of Geostationary Korea Multi-Purpose Satellite (GEO-KOMPSAT-2, GK-2) series was undertaken using both statistical and deep neural network (DNN)-based methods. The GK-2 mission includes an Advanced Meteorological Imager (AMI) onboard GK-2A and a Geostationary Environment Monitoring Spectrometer (GEMS) and Geostationary Ocean Color Imager-II onboard GK-2B. The statistical fusion method, Maximum Likelihood Estimation (MLE), corrected the bias of each aerosol product by assuming a Gaussian error distribution, and accounted for pixel-level uncertainties by weighting the root-mean-square error of each AOD product for every pixel. A DNN-based fusion model was trained to target Aerosol Robotic Network AOD values using fully connected hidden layers. The MLE and DNN AOD outperformed individual GEMS and AMI AOD datasets in East Asia (R = 0.888; RMSE = −0.188; MBE = −0.076; 60.6% within EE for MLE AOD; R = 0.905; RMSE = 0.161; MBE = −0.060; 65.6% within EE for DNN AOD). The selection of AOD around Korean peninsula, which is incorporating all aerosol products including GOCI-II resulted in much better results (R = 0.911; RMSE = 0.113; MBE = −0.047; 73.3% within EE for MLE AOD; R = 0.912; RMSE = 0.102; MBE = −0.028; 78.2% within EE for DNN AOD). The DNN AOD effectively addressed the rapid increase in uncertainty at higher aerosol loadings. Overall, fusion AOD (particularly DNN AOD) showed improvements with less variance and a negative bias. Both fusion algorithms stabilized diurnal error variations and provided additional insights into hourly aerosol evolution. The application of aerosol fusion techniques to future geostationary satellite projects such as TEMPO, ABI, and GeoXO may facilitate the production of high-quality global aerosol data.

1 Introduction

Since the launch of the Advanced Very High-Resolution Radiometer (AVHRR) onboard the US National Oceanic and Atmospheric Administration (NOAA) satellite, various atmospheric aerosol remote sensing techniques have been developed using spaceborne sensors (Kaufman et al., 1990; King et al., 1999). Radiometers such as the AVHRR, the MODerate resolution Imaging Spectroradiometer (MODIS), and the Visible Infrared Imaging Radiometer Suite (VIIRS) observe spectral bands across the visible (VIS) to infrared (IR) range. Several algorithms have been developed for these instruments to quantify aerosol optical depth (AOD) on a global scale. The Dark Target (DT; Kaufman et al., 1997; Remer et al., 2005; Levy et al., 2013) and Deep Blue (DB; Sayer et al., 2013; Hsu et al., 2006, 2013) algorithms, designed for aerosol optical property retrieval from MODIS, have established a global standard for spaceborne AOD products. The Multi-Angle Implementation of Atmospheric Correction (MAIAC) conducts spatiotemporal combinations of observations to facilitate aerosol retrieval and atmospheric correction (Lyapustin et al., 2011a, b; 2012; 2018). These algorithms have also been adapted for use with the VIIRS, which has similar observation specifications to those of MODIS. The Multiangle Imaging Spectroradiometer (MISR) measures surface radiance from nine viewing angles, enabling aerosol optical property inversion, and providing much information about different aerosol types (Kahn et al., 2001). Previous studies have exploited the sensitivity of hyperspectral imaging capabilities in the ultraviolet (UV) to VIS range of instruments such as the Total Ozone Mapping Spectrometer (TOMS), the Ozone Monitoring Instrument (OMI), and the TROPOspheric Monitoring Instrument (TROPOMI) to detect absorbing aerosols such as smoke and dust (Torres et al., 1998, 2002, 2020; Ahn et al., 2014). These aerosol retrieval algorithms involved the UV Aerosol Index (UVAI) in identifying aerosol types and derive AOD using pre-computed reflectance for the selected aerosol type; the algorithms employed by these instruments provide AOD as well as information on single scattering albedo (SSA), aerosol layer height (ALH), and above-cloud AOD (Torres et al., 2012; Jethva et al., 2018). The Deep Space Climate Observatory (DSCOVR) is located at the Lagrange-1 point, allowing continuous observation of Earth's sunlit area. The Earth Polychromatic Imaging Camera (EPIC) onboard DSCOVR features 10 bands spanning 317–779 nm. Lyapustin et al. (2021) demonstrated the capability of MAIAC in retrieving AOD and SSA from such instruments and further quantified the content of iron oxide in atmospheric mineral dust (Go et al., 2022).

For the Geostationary Earth Orbit (GEO) observations in Asia, the GEO-Kompsat-1 (GK-1) satellite, also known as the Communication, Ocean, and Meteorological Satellite (COMS) was launched in June 2010, equipped with a Meteorological Instrument (MI) and a GOCI (Kim et al., 2007; Lee et al., 2010b). The first satellite of the second series, GK-2A, was launched in December 2018, featuring an Advanced Meteorological Imager (AMI; Kim, D. et al., 2021). GK-2B was launched in February 2020, carrying the successor to GOCI (GOCI-II) and a Geostationary Environment Monitoring Spectrometer (GEMS) (GOCI-II ref; Kim et al., 2020; Choi et al., 2021). As the retrieval skill of the aerosol algorithm for GK-1 has well been established (Kim et al., 2008; Lee et al., 2010b; Kim et al., 2016; Choi et al., 2016, 2018), the instruments onboard GK-2 continue aerosol monitoring with improved observation specifications. For GEMS, as the first geostationary hyperspectral

spectrometer, an aerosol algorithm based on a two-channel inversion with an optimal estimation approach has been developed (Kim et al., 2018).

65 Aerosol retrieval algorithms vary in their application with the spectral specifications of the sensors they use. Employing multiple channels within the VIS to near-infrared (NIR) range enables aerosol inversion to capture information on aerosol size (Lin et al., 2021), whereas UV–VIS spectral observations are sensitive to aerosol absorption and layer height (Kim et al., 2018). Variability of instrument sensitivity leads to distinct error characteristics in aerosol algorithms. For example, retrieval algorithms utilizing wavelengths less sensitive to ALH tend to be robust against assumptions about ALH during radiative

70 transfer simulations. Moreover, observations across different wavelength ranges influence the spatial coverage of retrievals. As aerosol loading increases over a dark surface, atmospheric backscattering intensifies, causing more photons to reach satellite instruments. Conversely, over a bright surface, an elevated aerosol loading obscures signals reflected from the surface. The balance, where the increase in backscatter and disturbance of surface signals align, is termed the critical reflectance, which decreases with increasing wavelength (von Hoyningen-Huene, et al. 2011; Kim et al. 2014). As most land surfaces have lower

75 reflectance at shorter wavelengths, aerosol retrieval at such wavelengths results in broader spatial coverage.

Previous studies have shown that the use of multiple aerosol products addresses a systematic error tendency in AOD retrieval. MLE merging of AOD data from two or more satellites (or algorithms) has been explored in enhancing the accuracy of AOD quantification. Levy et al. (2013) and Wei et al. (2019) produced a merged MODIS DT–DB AOD product, accounting for systematic biases from each algorithm. Tang et al. (2016) employed the Bayesian maximum entropy method to merge AOD

80 from MODIS and Sea-viewing Wide Field-of-view Sensor (SeaWiFS) while considering the retrieval uncertainties associated with each AOD product. The optimal interpolation method iteratively updates AOD, factoring in MODIS, SeaWiFS, and MISR AOD uncertainties (Xue et al., 2014). Gupta et al. (2008) considered the point-spread function of each satellite footprint as a weighting factor for the merging of AOD from MODIS, MISR, and Clouds and the Earth's Radiant Energy System (CERES). The Maximum Likelihood Estimation (MLE) technique, which maximizes a cost function defined by the Gaussian error

85 distribution of satellite AOD products, is widely used in merging AOD data. This method was applied by Xu et al. (2015) to MODIS, SeaWiFS, and MISR data, and by Go et al. (2020) to OMI and MODIS data, accounting for uncertainties in each pixel. Xie et al. (2018) improved the methodology by correcting the systematic biases of the Advanced Along-Track Scanning Radiometer (AATSR). aerosol algorithms. Lim et al. (2021) employed the MLE method in considering pixel-level uncertainty and bias correction, resulting in merged AOD products from Advanced Himawari Imager (AHI), Geostationary Ocean Color

90 Imager (GOCI), and TROPOMI systems.

Most satellite AOD data-fusion research has concentrated on Low Earth Orbit (LEO) satellite data with limited consideration of GEO data. Unlike the LEO satellites, hourly variations in retrieval uncertainty emerge when using continuous AOD data from GEO satellites, and accounting for diurnal variations in uncertainty in aerosol data fusion is challenging. Furthermore, error characteristics among different AOD products under different retrieval conditions complicate matters. Deep learning

95 excels in capturing nonlinearities owing to its hierarchical architecture and activation functions in each layer, so a deep neural network (DNN) approach may significantly enhance AOD fusion outcomes. However, exploration of deep learning approaches

3

to AOD data fusion has been limited. In this study, both a conventional MLE AOD fusion algorithm and a DNN-based AOD fusion algorithm have been developed and validated using aerosol products from GK-2 satellites. Due to differences in spatial domain of each instrument, fused datasets are validated separately in a region around the Korean peninsula (KO) and a region within the East Asia (EA). Section 2 briefly introduces the spaceborne AOD datasets used in this study, derived from aerosol retrieval algorithms and an AERONET AOD dataset. Each fusion method is described in Section 3, and Section 4 discusses the fused AOD products based on diagnostic and prognostic error analysis. Finally, Section 5 provides a summary of the overall results and outlines prospects for geostationary aerosol data fusion.

2 Data

2.1 GK-2 Satellite instruments

An overview of instruments onboard GK-2 satellites and their aerosol products is provided in Table 1, and Fig. 1 illustrates the data coverage of each aerosol product.

2.1.1 AMI/GK-2A

As a meteorological imager, AMI has spectral channels in the VIS–IR range (Kim et al., 2021), which is 3 VIS channels, 1 near-IR channel, and 10 IR channels from 0.47 μm to 13.3 μm. A 0.65 μm channel has 0.5 km spatial resolution, and 0.47, 0.51 μm channels has 1.0 km spatial resolution. The IR channels has 2.0 km spatial resolution. AMI scans full-disk every 10 minutes, and local area near Korean peninsula every 2 minutes. Similar to conventional aerosol algorithms for instruments with VIS–IR capabilities, such as MODIS, VIIRS, AHI, and Advanced Baseline Imager (ABI), the AMI aerosol algorithm employs the VIS and NIR channel for aerosol inversion while utilizing other channels for bright surface masking and surface reflectance estimation.

2.1.2 GOCI-II/GK-2B

GOCI-II, onboard the GK-2B, is a second generation instrument of GOCI. Compared to GOCI, GOCI-II features a better ground sampling distance, an extended field of regard covering the hemisphere, and more spectral bands covering wavelength from 380 to 865 nm. GOCI-II has 4 additional bands (380, 520, 620, and 709 nm) compared to GOCI. Moreover, a wideband channel of GOCI-II is used for star imaging to improve image navigation and registration quality. Image acquisition of GOCI-II around the Korean peninsula (2500 km × 2500 km) is done by scanning 12 slots 10 times per day.

4

2.1.3 GEMS/GK-2B

GEMS is the first UV-VIS hyperspectral instrument on GEO orbit. GEMS is designed to monitor air quality in Asia (5°S–45°N, 75–145°E). GEMS observes reflected hyperspectral solar radiance from 300 to 500 nm wavelength range with a spectral resolution of 0.6 nm and a spatial resolution of 3.5 km × 7.7 km. GEMS scans sunlit part of the Earth during daytime. To obtain qualitative radiance data considering solar zenith angle, GEMS has 4 scanning scenarios of half-east, half-Korea, full-center, and full-west (Fig. 1). Since aerosol retrieval quality at high solar zenith angle depreciates, the half-east scan data, which is performed in the early morning, is not used for aerosol fusion study.

2.2 Aerosol retrieval algorithms for GK-2 instruments.

2.2.1 Yonsei aerosol retrieval algorithm (AMI, GOCI-II)

Lim et al. (2018) introduced the AHI Yonsei Aerosol Retrieval (YAER) algorithm, which was initially devised for ocean-color imagers. In this study, the AMI aerosol product was retrieved using the AHI YAER algorithm with minor modifications (Kim et al., 2024). The AMI YAER algorithm has two AOD retrieval versions based on different surface reflectance estimation methods; i.e., the Minimum Reflectance Method (MRM) and the Estimated Surface Reflectance (ESR) method. The distinct advantages of AMI for aerosol retrieval include more accurate cloud and bright surface masking via its IR channels compared with other instruments. Furthermore, its Short-Wave Infrared (SWIR) observation capabilities enable the use of the ESR method for surface estimation, offering uncertainty characteristics that are distinct from those of the MRM. Ocean surface reflectance estimation uses the Cox and Munk method (Cox and Munk, 1954) to estimate water leaving radiance with consideration of wind speed and chlorophyll-a concentration. In addition, the AMI has high temporal resolution, with full-disk scans every 10 min. For the purpose of aerosol data fusion, a domain spanning 10°S–50°N and 70°E–150°E of the AMI full-disk scan was chosen to encompass the GEMS field of regard.

GOCI-II aerosol product is derived from the GOCI-II YAER algorithm (Lee et al., 2023) based on the GOCI YAER algorithm introduced by Lee et al. (2010b) and improved by Choi et al. (2016, 2018). The enhanced spatial resolution of GOCI-II compared to GOCI allows its aerosol products to be retrieved at a resolution of 2.5 km, capturing higher-resolution spatial aerosol features around the Korean peninsula. However, the smaller field of regard of GOCI-II restricts AOD fusion to within the GOCI-II domain when using aerosol products from all three instruments. Consequently, fusion AOD utilizing all three aerosol products was evaluated separately (Section 4). Due to the absence of SWIR channels, the GOCI-II YAER algorithm estimates surface reflectance using only the MRM, with the concentration of 12 spectral bands within the UV–NIR range contributing to the stability of AOD inversion. Ocean surface reflectance estimation is done as the same manner for AMI YAER algorithm using the Cox and Munk method.

Aerosol size influences the spectral dependency of AOD within the UV-NIR spectral range. Therefore, both AMI and GOCI-II are sensitive to the potential misclassification of aerosol types related to their size. However, their reduced sensitivity to

aerosol absorption in the VIS range renders the YAER AOD products robust against uncertainties arising from aerosol absorptivity. Both the AMI and GOCI-II YAER algorithms consider four types of aerosol: black carbon (BC), non-absorbing (NA), mixed (MX), and dust (DU) aerosol. Aerosol models utilized in the YAER algorithms were derived from climatology of AERONET inversion dataset with the classification developed by Lee et al. (2010a). The YAER algorithm first retrieves AODs at all wavelengths within UV-NIR range and converted to 550 nm for all aerosol types. Then, aerosol type that shows minimum variance at 550 nm are selected aerosol type for the corresponding inversion pixel.

2.2.2 GEMS Aerosol retrieval algorithm

The GEMS aerosol algorithm was initially developed by Kim et al. (2018) and Go et al. (2020) based on synthetic data from OMI observations. The operational GEMS aerosol algorithm, based on real observations, was subsequently established by Cho et al. (2023). GEMS performs hourly hyperspectral radiance observations of 300–500 nm with 0.6 nm spectral resolution during daytime. Its spatial resolution at nadir point is 3 km × 7.7 km. Distinct from other instruments on GK-2 satellites, GEMS features near-UV measurement that can be utilized for aerosol inversion. The optically darker nature of desert surfaces in near-UV measurement serves as a favorable condition for the retrieval of aerosol signals from observed radiance. This allows unprecedented hourly aerosol monitoring over desert regions such as the Gobi and Taklamakan deserts. Furthermore, near-UV spectral region is known to be sensitive to aerosol absorption, contributing to distinct error characteristics in GEMS AOD relative to AMI and GOCI-II. In this study, a version 2 of the GEMS AOD at 550 nm was used to maintain consistency with AMI and GOCI-II AOD products. A version update of the GEMS aerosol algorithm was made public in November 2022, and earlier data were reprocessed accordingly.

Unlike the AMI and GOCI-II YAER algorithms, tThe GEMS is more sensitive to misclassification of absorbing/scattering aerosol types. The GEMS aerosol retrieval algorithm initially performs aerosol type selection with UV aerosol index (UVAI) and VIS aerosol index (VISAI). The algorithm assigns NA type to pixels with low UVAI values. The other pixels are separated into highly-absorbing fine (HAF) type and DU type according to the VISAI values. The aerosol type classification of the GEMS AOD retrieval is superior to the other algorithms using visible wavelengths because of the sensitivity of UV wavelength to scattering characteristic of aerosols. Yet, relatively short range of observation wavelength in VIS region of GEMS compared to AMI and GOCI-II lacks sensitivity to aerosol size information. Then After the aerosol type classification, the algorithm performs a two-channel inversion used in OMI near-UV aerosol algorithm to derive first guess of AOD and SSA. Then, the first guesses are fed into the GEMS optimal estimation algorithm to retrieve AOD at 443 nm. The 443 nm AOD is converted to 550 nm AOD based on the selected aerosol type.

2.3 AERONET

The AErosol RObotic NETwork (AERONET) constitutes a global network of ground-based aerosol remote sensing instruments, with numerous sun photometer stations operating at various locations worldwide. The AERONET level 1.0 data

6

are unscreened measurement data. The cloud and pointing error screening is applied to level 1.0 data to produce a level 1.5
dataset. The level 1.5 data series are raised to level 2.0 (quality-assured) series after final calibration values are applied and
manual data inspection is completed. Here, AERONET version 3, level 2.0 AOD products served as the target AOD for both
MLE and DNN-based methods (Section 3). However, in the validation of individual and fused AODs (Section 4), AERONET
version 3, level 1.5 AODs were used owing to the limited application of pre- and post-calibration for only a few sites up to
2023; therefore, level 1.5 AODs were more suitable for validating relatively recent data. The estimated uncertainty in precision
in AERONET AODs is known to be 0.010–0.021 depending on the wavelength (Holben et al., 1998; Eck et al., 1999; Giles et
al., 2019; Sinyuk et al., 2020). Over the course of the error analysis and training period, 74 stations reported ground-based
level 2.0 AOD data. For the validation period, 91 stations reported ground-based level 1.5 AOD, including 28 stations within
the field of regard of GOCI-II. Table 2 lists the AERONET sites used in the study. To match AOD wavelengths with those of
spaceborne AOD products, the AERONET 550 nm AOD was derived through quadratic interpolation from AODs measured
at 340, 380, 440, 500, 675, 870, and 1020 nm. For spatiotemporal matching with AERONET measurements, satellite data
within a 25 km radius of each AERONET site were averaged, and AERONET AODs within 30 min of each exact hour were
also averaged for spatiotemporal collocation (Park et al., 2020).

3 Methodology

A flowchart of MLE fusion and DNN-based fusion processes is shown in Fig. 2. Each of these fusion methods requires a pre-
calculation process involving bias and uncertainty calculations for MLE fusion and a model training process for DNN fusion.
Data spanning one year (November 2021 to October 2022) were used in pre-calculation processes. The resultant fused AODs
were generated and validated for the period November 2022 to April 2023. Throughout data pre-calculation, AERONET AOD
served as the reference ground truth for both fusion methods. The AMI Normalized Difference Vegetation Index (NDVI) was
used as both an uncertainty source and an input for both fusion approaches, as calculated using Eq. (1):

$$NDVI = \frac{R_{red} + R_{NIR}}{R_{red} - R_{NIR}} \qquad (1)$$

where R represents AMI MRM surface reflectance. The MRM surface reflectance was used because aerosols may affect the
NDVI when using observed reflectance. Spatiotemporal matching of AMI NDVI followed the same approach as AMI AOD.
Henceforth, for the sake of simplicity, the statistically fused AOD is referred to as MLE AOD, and the DNN-based fused AOD
as DNN AOD.

3.1 Spatiotemporal matching and additional cloud masking with AMI IR observations

Because each instruments observes the Earth radiance with distinct geolocation fields, the geolocations of aerosol products are
different. Therefore, aerosol products were re-gridded into 0.05° × 0.05° grids by averaging AOD values from the three closest
pixels located within a 0.15° radius of the center of each grid point. The choice of a 0.15° radius was intended to prevent grid
pixels from becoming empty owing to the coarsening of spatial resolution near the scan edge (as in western China). However,

7

220 this approach may lead to smoothing of aerosol features in regions distant from scan edges. To counteract excessive smoothing and preserve small aerosol features after re-gridding, the strategy involved averaging the maximum three points regardless of how many points lay within the specified averaging radius. This spatial matching technique was intended to provide a balance, mitigating excessive smoothing while retaining finer aerosol features. The re-gridded aerosol products are also used for error analysis and DNN model training to account for small errors may induced from the re-gridding process.

225 Given the distinct scanning scenarios of each sensor, a distinct temporal matching strategy was employed for each AOD product to generate AODs for every precise hour between 00:00 UTC and 07:00 UTC. For temporal matching of 04:00 UTC fusion, GEMS AOD data scanned from 03:45 UTC to 04:15 UTC were utilized as the AOD representation for 04:00. In the case of AMI AOD, data were collected for a time span of 03:30−04:30 UTC from each precise hour and a median AOD was calculated. As for GOCI-II, data scanned at 03:15 and 04:15 were simply averaged.

230 Aerosol retrieval algorithms inherently include a cloud masking process; however, GEMS and GOCI-II cloud masking may exhibit errors owing to challenges in distinguishing thin clouds such as cirrus from aerosols using only VIS channels. Therefore, a cloud detection database employing IR channels was extracted during the AMI YAER algorithm retrieval process and applied to the GEMS and GOCI-II aerosol products. The cloud-masking criteria of the AMI YAER algorithm are shown in Table 3, where the first two criteria in the list utilize the fixed geometry of GEO satellites. Because clouds change rapidly with time,

235 the maximum brightness temperature (BT) within the previous 10 days served as an estimate of BT on a clear day. Pixels displaying a difference between maximum BT during the 10 days and observed BT in the 6.9 and 11.2 μm channels of less than −28 K were thus identified as cloud pixels. This method was introduced by Kim et al. (2014) using MI and has proved effective and reliable with AHI (Lim et al., 2018). The 1.38 μm channel is highly sensitive to cirrus clouds (Roskovensky and Liou, 2003), so pixels exhibiting a top-of-atmosphere reflectance exceeding 0.35 in the 1.38 μm channel were masked as

240 clouds. Detection of lower clouds involved the brightness-temperature difference (BTD) of the 13.3 and 10.3 μm (known as the "atmospheric window") bands (BTD10.3–13.3). Over clear pixels, the BT of the 13.3 μm channel is significantly lower than that of the 10.3 μm channel due to well-mixed CO_2 in the troposphere, resulting in a substantial BTD10.3–13.3. The presence of clouds reduces BTD10.3–13.3, as the BT of the 10.3 μm channel is lower in cloud pixels. The detection of higher clouds followed a similar approach utilizing the 12.3 μm channel, which is sensitive to high-altitude water droplets and ice

245 crystals. The IR-based masks applied to GOCI-II and GEMS AODs were implemented across all aspects of the study including error analysis, bias and uncertainty calculations, and DNN model training.

The effects of a cloud mask in refining GEMS and GOCI-II AOD are shown in Fig. 3, where yellow boxes indicate cloud-free regions that were not removed by the additional cloud mask, and magenta boxes highlight regions where the original GEMS or GOCI-II aerosol algorithms inaccurately detected clouds, leading to overestimated AOD values. An example for 25

250 November 2022, over the arid region of northern China, is depicted in Fig. 3a–c; the Taklamakan desert is highlighted by the yellow box in Fig. 3a. In comparing the original GEMS AOD with that after application of the AMI IR cloud mask (Fig. 3b– c), it is evident that the cloud mask did not mistakenly classify bright surfaces as clouds. The magenta box in Fig. 3b indicates areas where the GEMS aerosol algorithm retrieved AOD values over thin clouds, leading to significantly elevated values of

8

up to 1.2, while values near the clouds remained below 0.2. Some pixels even had AOD values exceeding 2.0. These problematic pixels were removed in Fig. 3c, leading to spatially consistent AOD results for GEMS after application of the additional cloud mask. The additional cloud mask was applied to GOCI-II AOD on 9 March 2023 (Fig. 3d–f), when a substantial aerosol plume was being transported across the Southern Ocean toward the Korean peninsula. The hazy atmosphere extended over Japan and into the western Pacific Ocean. However, the GOCI-II YAER algorithm failed to accurately detect thin clouds (magenta box, Fig. 3e). Application of the AMI IR cloud mask (Fig. 3f) effectively removed cloud-contaminated AOD values. The yellow box (Fig. 3d) highlights a dense aerosol plume. GOCI-II AOD values over the plume remained intact after application of the additional cloud mask, demonstrating that the cloud mask based on IR channels was proficient in distinguishing thin clouds from thick aerosol plumes.

3.2 Statistical aerosol fusion: MLE AOD

MLE aerosol data fusion employed an MLE method that accounted for the pixel-level uncertainty of each aerosol product. The MLE method operates under the assumption that its input AODs have unbiased random errors. Typical AOD distributions, which are often lognormal, tend to have a Gaussian uncertainty distribution (Sayer et al., 2020). However, the actual mean error does not always coincide with zero, contradicting the assumption made by the MLE method. To enhance the MLE input data quality, a preliminary bias correction for each AOD product was undertaken before initiating the fusion process. Here, AOD bias was defined as the mean of a Gaussian distribution fitted to the AOD error, as compared with the collocated AERONET AOD. To account for bias characteristics attributed to optical path variations and surface conditions, AOD bias values were computed for each hour, aerosol type, and NDVI bin.

Based on a zero-mean Gaussian error assumption after bias correction, a log-likelihood function $\rho(\tau)$ was written as follows:

$$\rho(\tau) = \sum_i \frac{1}{R_i \sqrt{2\pi}} \left(-0.5 \left(\frac{\tau - \tau_i}{R_i} \right)^2 \right),$$ (2)

where τ_i is a bias corrected AOD from instrument i, and R_i is the uncertainty of τ_i. Then, a derivative of the above log-likelihood function was written as follows:

$$\frac{\partial \rho(\tau)}{\partial \tau} = \sum_i \frac{\tau - \tau_i}{R_i^2}.$$ (3)

Finally, the AOD that maximized the log-likelihood function had a τ value that made the above derivative zero:

$$\tau = \frac{\sum \tau_i R_i^{-2}}{\sum R_i^{-2}}$$ (4)

The above Eq. (4) can be interpreted as an uncertainty-weighted mean of AOD products. Here, the uncertainty associated with each aerosol product was represented by the root-mean-square error (RMSE) of the AOD products relative to AERONET AOD measurements. As shown in Fig. 5-7, retrieval error does not increase (or decrease) linearly. Therefore, merging AOD

9

datasets using the same RMSE value for all pixels is not desirable. The MLE fusion method linearizes the error characteristics by categorizing potential error sources such as AOD values, aerosol types, NDVI values, and observation times. The potential

285 error source variables are selected based on the following logistics. First, AOD value itself and aerosol type is selected because as aerosol loading increases, aerosol model assumption affects retrieval performance. Complex aerosol mixture at high aerosol loading leads to high uncertainty and aerosol retrieval algorithms have distinct aerosol model assumptions. NDVI is selected as possible error source to represent surface condition. Different surface types have different surface reflectance and surface types differentiate by vegetation amount and types (Hsu et al., 2013). Observation time difference in GEO measurements leads

290 to distinct optical path of observed radiance. Therefore, GEO satellite AOD products have diurnal error variations (Lim et al., 2018; Zhang et al., 2020; Fu et al., 2023; Cho et al., 2024). To deal with the uncertainty from this, observation time is selected as the possible error source. Based on this analysis, the bias of each AOD product was subtracted according to the NDVI value, selected aerosol type (ancillary output of each aerosol products), and observation time. Following this bias correction, the RMSE for the MLE procedure was computed. The output of the fusion process was then categorized in accordance with AOD

295 data availability, as shown in Table 4.

3.3 Deep neural network-based aerosol fusion: DNN AOD

A DNN is a powerful tool for capturing non-linear relationships among physical variables. Although ground-based and spaceborne AODs exhibit linear relationships owing to their fundamentally similar physical meanings, their error characteristics under diverse retrieval conditions can introduce nonlinearity. The MLE AOD fusion method attempts to address

300 this nonlinearity by considering pixel-level uncertainty associated with each aerosol product. However, certain unexplained nonlinearities remain, and a DNN-based AOD fusion algorithm was formulated as follows.

The DNN model was constructed to predict AERONET AOD as the target variable, employing the same input data as the MLE AOD fusion approach. To improve model convergence and enhance the overall performance of the DNN, a preprocessing step was necessary for the input data. This involved standardization of the NDVI, hour, and aerosol type index (for GEMS, 1

305 = HAF, 2 = DU, 3 = NA; for AMI and GOCI-II, 1 = BC, 2 = NA, 3 = MIX, 4 = DU). The standardization process was implemented using Eq. (5):

$$x_{input} = \frac{x - \mu_x}{\sigma_x}, \tag{5}$$

where μ_x and σ_x represent the mean and standard deviation of input data x, respectively. The AOD follows a lognormal distribution skewed toward higher values. To address this distribution characteristic, a Box–Cox transformation was

310 implemented for standardizing AOD products derived from the three instruments and AERONET. This transformation, based on the concept initially introduced by Tukey (1957), has been adapted and shown to be effective for data normalization (Box and Cox, 1982; Sakia, 1992).

A simplified architecture of a fully connected feed-forward neural network model is illustrated in Fig. 2. This DNN model comprises three hidden layers, with each being fully connected. Within each hidden layer, batch normalization was

10

315 implemented to avoid overfitting by bringing numerical data onto a common scale. In addition, the rectified linear unit (ReLU) served as the activation function. Weighting coefficients of the neural network were optimized by minimizing the mean-square-error (MSE) loss. During training, the backpropagation technique was applied, adjusting the weight coefficients based on the gradient of the loss function. Hyperparameters including batch size, number of neurons, and learning rate were determined using the asynchronous successive halving algorithm (ASHA; Li et al., 2020). For the ASHA optimization process, a maximum

320 of 1000 trials were set, with a minimum of 100 trials. In each trial, half of the configurations were eliminated. Following optimization, the DNN model was trained for each case of AOD availability, as outlined in Table 4.

4 Results and discussion

4.1 Error analysis of GEMS, AMI, and GOCI-II AOD products.

Error analysis of original AOD products gives intuition of expected contributions of each AOD products and helps to interpret

325 the outcome. Here, we used spatiotemporally matched AOD products to minimize the effect of re-gridding and temporal matching to the input AOD value. Wavelength of AOD used for error analysis and data fusion are at 550 nm. Also, additional IR cloud masking is applied to GEMS and GOCI-II AOD products. Fig. 4 depicts 2-dimensional histograms illustrating the match between individual AOD products and AERONET AOD measurements. The expected error envelope (EE envelope; $\pm(0.05 + 0.15 \text{AOD})$) of AOD was established by Levy et al. (2013). GEMS AODs exhibited a tendency to underestimate AOD

330 at high aerosol loadings (Fig. 4a), with a slope of 0.429 relative to AERONET AOD. Cho et al. (2023) reported that the latest version of GEMS AOD at 443 nm does not have such a low slope, implying that the underestimation of GEMS 550 nm AOD in the version 2 algorithm may be due to either an algorithm issue or errors during wavelength conversion. Despite this underestimation, GEMS AODs were strongly correlated with AERONET AODs, with a Pearson's correlation coefficient (R) of 0.715. GOCI-II AODs yielded the most comparable outcomes to AERONET AODs among the four aerosol products (Fig.

335 4b). The stable inversion of AOD achieved through utilizing 12 UV–NIR channels likely contributed to the robustness of the GOCI-II YAER algorithm. The Mean Bias Error (MBE) of GOCI-II AODs was negative, mainly because of a clustering of slight underestimations at low aerosol loadings. This underestimation at low AOD is a known issue when using MRM surface reflectance because of the assumption that at least one aerosol-free day exists within a 30-day period, which is not universally valid because of background AOD as indicated in Lee et al. (2023). A comparable issue with low aerosol loadings was evident

340 with AMI–MRM AOD (Fig. 4c). Both AMI–MRM and AMI–ESR AODs (Fig. 4c–d) displayed scattered patterns relative to GOCI-II AODs. The overestimation of low AOD values observed in both AMI–MRM and AMI–ESR AODs may be attributed to insufficient cloud masking over land. Comparison of the two AMI AOD products indicated that AMI–ESR AOD yields slightly superior outcomes, likely because of the enhanced surface reflectance estimation over urban regions with the ESR method, as indicated in previous studies (Lim et al., 2018; Kim, M. et al., 2021).

345 The biases in GEMS AOD products with AOD, NDVI, aerosol type, and observation time are illustrated in Fig. 5, where blue numbers in each plot indicate the count of collocated data in the respective box–whisker, and green dashed lines in each panel

11

correspond to the y-axis range of the corresponding panels in the GOCI-II error analysis (Fig. 6). As AERONET AOD values increased, the GEMS AOD acquired an increasingly negative bias. Conversely, at low aerosol loadings (AERONET AOD < 0.2), GEMS AOD displayed a positive skewness, implying that it tends to overestimate low AOD values while simultaneously

350 overestimating high AOD values. Where NDVI < 0.5, the error in GEMS AOD consistently demonstrated a negative skewness and bias. However, in high-NDVI regions, usually associated with dark surfaces, the bias is nearer zero. The negative error of GEMS AOD for HAF aerosols may be induced by errors in aerosol optical properties of the model (Cho et al., 2023). However, aerosol type selection is not absolutely independent of surface conditions. In winter, the NDVI in Southeast Asia falls to 0.3– 0.4 (Ji et al., 2017), with massive HAF aerosols being emitted by biomass burning (Yin, 2020). Then, GEMS AOD displays

355 an M-shaped diurnal variation that is consistently negatively biased, except for at 01 UTC. Diurnal variations in GEMS AOD may be influenced by the relatively short atmospheric path length at noon (04 UTC). Furthermore, variations among collocated AERONET sites, which are due to differing scan scenarios throughout the day, may also contribute to the observed diurnal error variations.

The same error analysis applied to GOCI-II AOD is illustrated in Fig. 6. The GOCI-II AOD error relative to AERONET AOD

360 displayed a pattern of underestimation with increasing aerosol loading (Fig. 6a), although the magnitude of this error was notably smaller than that observed with GEMS AOD. In terms of NDVI (Fig. 6b), GOCI-II AOD seemed to exhibit consistent behavior regardless of land surface conditions. Over ocean areas (NDVI <0) the GOCI-II YAER algorithm delivered unbiased retrievals, and bias characteristics were similar across different aerosol types. The MX-type aerosol (the most frequently selected type in the GOCI-II YAER algorithm) yielded the most stable results with the shortest range of whiskers (Fig. 6b).

365 Conversely, the NA aerosol had the greatest whisker range, indicating potential issues with the NA model in the algorithm. Asian dust is associated with high aerosol loadings, and results for DU aerosols are slightly more negative (Fig. 6c). Diurnal variations in GOCI-II error appeared stable, with slight underestimation during mornings and late afternoons. As the GOCI-II field of regard is smaller than those of GEMS and AMI, geometrical conditions may have had less impact on its performance. Error analysis results for the two versions of AMI AODs are depicted in Fig. 7, which shows that both AMI–MRM (Fig. 7a)

370 and AMI–ESR (Fig. 7e) AOD biases tend to decrease with increasing AERONET AOD values. This bias pattern may be attributed to the difference in surface reflectance estimation methods used by the two AOD versions. This distinction became more evident with low aerosol loadings, where the surface signal contributes substantially to the observed radiance. A comparison of the initial box–whisker plots for each AMI AOD version suggested that the AMI–ESR AOD bias is closer to zero with low aerosol loadings. Furthermore, the shorter lengths of the box–whisker plots across various NDVI values (Fig.

375 7f) indicate that the AMI–ESR YAER algorithm provided a more consistent estimate of surface reflectance than that of the AMI–MRM YAER. Considering that both versions of the AMI YAER algorithm employ the same aerosol models, the variations in AOD bias between the two were similar (Fig. 7c, g). The diurnal error variation (Fig. 7d, h) was not notably different between the two AMI AOD products. This similarity in diurnal error variations suggests that the choice of surface-reflectance estimation method has limited impact on error characteristics based on observation time.

4.2 Fusion data evaluation

4.2.1 Validation of the fused AOD with AERONET

Based on the error analysis and DNN model training for the period from November 2021 to October 2022, AOD data were fused for six months spanning November 2022 to April 2023. The GOCI-II field of regard focusing on KO was smaller than those covering EA, so the fused AOD utilizing GOCI-II AOD was confined within the domain. Therefore, two groups of fused AOD products were generated: one involving the entire EA domain (AOD-EA), and the other focusing exclusively within KO (AOD-KO), which is the domain covered by GOCI-II. Validation results of both MLE and DNN-based fused AODs are shown in Fig. 8, where columns represent the validation results of MLE and DNN AODs, and rows denote the results for AOD-EA and -KO. Overall, the validation metrics exhibited notable improvement after the MLE fusion process (including bias correction and MLE fusion) relative to the results of individual GEMS and AMI AOD products (Fig. 8a). The MLE fusion significantly enhanced AOD quality (R = 0.888; RMSE = −0.188; MBE = −0.076; 60.6% within EE). In EA, DNN-based fusion outperformed the MLE fusion, with a substantial enhancement in AOD quality (R = 0.905; RMSE = 0.161; MBE = −0.060; 65.6% within EE). The improvement at low AOD contributed to the notable increase in the percentage of AOD values within the EE. Furthermore, DNN fusion seemed to improve the underestimation of GEMS and AMI AOD at high aerosol loading better than MLE fusion. Fused AOD incorporating data from all three satellite instruments (for AOD-KO) are depicted in Fig. 8c, d. Although the impact of high-AOD underestimation by GEMS and AMI influenced the MLE AOD results, the validation metrics were notably superior to those of individual satellite AOD products including GOCI-II (R = 0.911; RMSE = 0.113; MBE = −0.047; 73.3% within EE). By merging the original AOD dataset according to retrieval error compared to AERONET in different retrieval conditions (NDVI, observation time, aerosol loading and type), the MLE fusion approach thus effectively accommodated nonlinearity in retrieval uncertainty, despite possibly not capturing all complexity in the data. DNN-KO yielded more improved outcome (R = 0.912; RMSE = 0.102; MBE = −0.028; 78.2% within EE). As was in the validation of DNN-EA, the better result of DNN AOD comes from improvement in high AOD (AOD >0.5). Further incorporation of relevant information may enhance the performance of DNN AOD products, but such considerations are beyond the scope of this study. Validation results of the original AOD products and fused AOD in the separate regions of -EA and -KO are listed in Table 5 and Table 6.

4.2.2 Aerosol product evaluation

The prognostic error (or, uncertainty) evaluation methodology was based on the framework of Sayer et al. (2020). A comparison of 1σ retrieval error (68th percentile of absolute AOD error against AERONET, $|\Delta_S|_{68}$; 1σ of Gaussian distribution) according to AOD is shown in Fig. 9. The $|\Delta_S|_{68}$ values represent estimates of the AOD products' uncertainty. Fig 9a shows a prognostic error evaluation of AOD products in East. Asia (AOD-EA). At low AOD, the three original satellite AOD products (GEMS, AMI–MRM, AMI–ESR) displayed large uncertainty that is decreasing rapidly as AOD increases to 0.1. This implies that at low AOD values, the satellite AOD products had relatively high uncertainties, which can likely be attributed to weak

13

aerosol signals and/or cloud contamination issues. With increasing aerosol loading, the uncertainty gradually increases. Among the three original AOD products in EA, GEMS AOD demonstrated the largest uncertainty, which was 0.708 at AOD of 0.638. Uncertainty of the GEMS 550 nm AOD was even larger at 550 nm due to underestimation of AOD and error due to the extrapolation from 443 nm. The prognostic error of GEMS AOD at 550 nm in -EA region was estimated as 0.03 + 0.82AOD. The AMI–ESR AOD had lower uncertainty compared to GEMS AOD, and the AMI–MRM AOD products showed slightly larger uncertainty than AMI–ESR AOD. The prognostic error estimates of AMI–MRM and –ESR AOD product were 0.07 + 0.25AOD and 0.08 + 0.20AOD, respectively. The two fused AOD products in EA (triangle markers, Fig. 9a) indicate that aerosol fusion effectively reduced AOD uncertainty at lower aerosol loadings. As the loading increased, the uncertainties of both MLE-EA and DNN-EA AOD products showed similar retrieval errors as AOD increases to ~0.3. At higher aerosol loading, the MLE-EA AOD showed uncertainties in between GEMS AOD and AMI AODs. Meanwhile, uncertainties of the DNN-EA were even lower than AMI–ESR. The prognostic error estimates for MLE AOD and DNN AOD were 0.02 + 0.43 AOD and 0.05 + 0.23 AOD, respectively. AOD products in -KO region generally showed lower uncertainty than in -EA region (Fig. 9b). Among the four original AOD products, GOCI-II showed lowest uncertainty at high aerosol loading. In the KO, the two AMI AOD products had similar results. This seems to be because the effect of difference in surface reflectance estimation diminishes as the -KO domain contains AERONET sites (e.g., Beijing) with frequent severe haze events. However, relatively higher uncertainty at low aerosol loading still remains for AOD <0.1, even for GOCI-II. The prognostic error estimates for GEMS, GOCI-II, AMI–MRM, and AMI–ESR AOD products are 0.01 + 0.71AOD, 0.05 + 0.17AOD, 0.05 + 0.21AOD, and 0.06 + 0.19AOD, respectively. The MLE-KO AOD showed similar uncertainties with AMI AOD products at high aerosol loading with uncertainty estimate of 0.02 + 0.28AOD. However, the slope of the prognostic error was higher than AMI–MRM AOD because of lower uncertainty at low aerosol loading. Meanwhile, the DNN AOD-KO had the lowest uncertainties among all AOD products with uncertainty estimate of 0.03 + 0.18AOD.

Means and standard deviations of the normalized error (Δ_N) of AOD and fused AOD products are shown in Fig. 10, where the AOD error was normalized using Eq. (6):

$$\Delta_N = \frac{\Delta_S}{\epsilon_T} = \frac{\tau_S - \tau_A}{\sqrt{\epsilon_S^2 + \epsilon_A^2}} \cong \frac{\tau_S - \tau_A}{|\epsilon_S|} \tag{6}$$

where ϵ_T denotes a total expected discrepancy; i.e., a root of the squared sum of expected discrepancies of satellite and AERONET. Values of Δ_N with a Gaussian distribution of zero mean ($\mu_{\Delta N}$) and unity standard deviation ($\sigma_{\Delta N}$) implies that satellite AODs were calculated appropriately with perfectly characterized errors (Sayer et al., 2020). Here, the satellite expected discrepancy (ϵ_S) assumed to be the EE of MODIS DT land retrieval. Therefore, points near the intersection of mean zero and variance unity lines (Fig. 10) imply that the accuracy and precision of AOD product uncertainty can be explained by the EE of the MODIS DT.

Means and standard deviations of the normalized error of each AOD product collocated at four different AERONET sites are plotted in Fig. 10. Beijing_RADI and Anmyon sites represent polluted atmosphere over land and coast, respectively. Beijing is one of the largest cities in East Asia, and Anmyon is located near the Yellow Sea, over which long-range aerosol transport

14

445 passes (Lee et al., 2019). AERONET sites remote from large cities in Japan, TGF_Tsukuba and Okinawa_Hedo were selected to demonstrate results for relatively clear atmosphere over land and coast, respectively. Over the polluted land site, the original AOD products showed negative bias. AMI–MRM, AMI–ESR, and GOCI-II AOD had $\sigma_{\Delta N}$ close to unity, while that of the GEMS AOD was higher. Both fused AOD products had smaller $\sigma_{\Delta N}$ values than unity, meaning that the fused AOD products have higher precision than MODIS DT over polluted atmosphere. Among the two fused AOD, DNN showed better

450 performance with better accuracy ($\mu_{\Delta N}$ closer to zero) and higher precision (lower $\sigma_{\Delta N}$), due to better estimation of high AOD as shown in discussions regarding Fig. 8. Over clear land site, among original AOD products, GEMS AOD had highest precision and GOCI-II AOD had highest accuracy. Both AMI AOD products had low precision, with positive bias of AMI–MRM AOD and negative bias of AMI–ESR AOD. The MLE AOD showed improvement in precision but had positive bias after fusion. This seems to be because the bias correction procedure is applied regardless of AOD value. For the case of GEMS

455 AOD, small bias over clear atmosphere may be overcorrected to have positive bias before MLE fusion. DNN AOD does not seem to have such a problem, with even better precision than at the polluted site. AMI AOD collocated at the Anmyon site had a strong positive bias (Fig. 10b) due to overestimation of AOD over turbid water. Over clear coastal areas, AMI–MRM, AMI–ESR and GOCI-II AOD products displayed relatively high precision with positive bias. Cloud contamination may cause the positive bias. Over both coastal sites, MLE-KO AOD outperformed DNN-KO AOD. Relatively consistent retrieval

460 conditions of ocean surface than land surface may lead to better quantification of uncertainty for MLE fusion.

4.2.3 Diurnal variation during aerosol transport in East Asia

A case of long-range aerosol transport over the Yellow Sea is described in Fig. 11. A scattering aerosol plume originating from the Shandong Peninsula was transported toward Japan, penetrating South Korea. Three AERONET sites were chosen to assess diurnal variations of AOD during this event. The diurnal variations of AERONET AOD were similar at Yonsei_University

465 (37.6 °N, 126.9 °N) and KORUS_UNIST_Ulsan (35.6 °N, 129.2 °E) (Fig. 11b–c), characterized by a peak at around 01:30 UTC followed by a gradual decline throughout the day. At the Yonsei_University site (Fig. 11b), AERONET AOD data for the 00–02 UTC period were absent due to cloud cover. GEMS AOD exhibited a diurnal pattern similar to that of AERONET but, as established in earlier analyses, GEMS tends to underestimate AOD, particularly with high aerosol loadings. AMI–MRM AOD captured AERONET AOD well until 02 UTC, after which it underestimated AOD. AMI–ESR AOD displayed

470 similar trends but with the most negatively biased retrieval among all AOD products, consistent with the negative bias observed in error analysis (Fig. 7d, h). GOCI-II AOD demonstrated the most accurate performance during this event. After MLE fusion, MLE AOD closely followed the diurnal AOD variation of AERONET, with slight underestimation. Due to the greater uncertainty of GEM AOD under high aerosol loadings, its weight in the MLE fusion was lower than those of other satellite AOD products, with MLE AOD being more similar to other AOD products. The MLE fusion method successfully combined

475 each AOD product by considering retrieval uncertainties under various conditions. DNN AOD exhibited a closer value of AOD compared to MLE AOD, as expected based on former discussions. However, with DNN AOD, diurnal AOD variation may be misunderstood to be consistently increasing after 04 UTC, while the AERONET AOD is decreasing again after 05

15

UTC (Fig. 11b). Collocated results from the Gosan_SNU site (33.3 °N, 126.2 °E) (Fig. 11d), which was located outside the main plume, had a moderately high aerosol loading with an average AERONET AOD of ~0.4. GEMS consistently underestimated AOD throughout the day, whereas both AMI–AOD products overestimated AOD slightly in the early morning (00–02 UTC). Both MLE and DNN AOD showed almost the same AOD values throughout the day at Gosan_SNU site.

5 Conclusion

Individual AOD products from GEMS, AMI, and GOCI-II were validated over the period of November 2022 to April 2023 using AERONET level 1.5 AOD as a reference. Linear regression line of GEMS AOD and AERONET AOD exhibited a slope of 0.368, indicating underestimation of high aerosol loading relative to AERONET AOD. The GOCI-II YAER algorithm yielded better performance than GEMS and AMI. Within AMI YAER algorithms, the validation of AMI–ESR AOD was slightly more accurate than that of AMI–MRM AOD due to the better estimation of urban surface reflectance in the former. Two AOD data fusion methods were developed using the same input variables—GEMS, AMI (–MRM and –ESR), and GOCI-II AOD—with NDVI, observation time, and selected aerosol type from each algorithm. For MLE fusion, pixel-level biases and RMSEs of aerosol algorithms were calculated by comparing individual satellite AODs with level 2.0 AERONET AODs for November 2021 to October 2022, with this period being used also for DNN model training. Fusion outcomes were categorized into two groups based on the individual AODs used in fusion and then evaluated. The fused AOD-EA from both MLE and DNN-based fusion yielded better results relative to GEMS and AMI AOD products. DNN AOD outperformed MLE AOD, particularly in terms of quantifying AOD at high aerosol loading. Due to small spatial domain of the GOCI-II observation, fused AOD-KO was selected for evaluation of fusion involving GOCI-II AOD. Both MLE and DNN AOD-KO yielded better results than GOCI-II AOD. MLE AOD retained underestimation owing to the GEMS tendency to underestimate high aerosol loadings. This issue was not observed with DNN AOD-KO. Evaluation of AOD bias with respect to observation time indicated that both fusion algorithms stabilized diurnal error variations, suggesting that fusion AOD enhances our understanding of the hourly evolution of aerosol distributions. The performance of each AOD product was assessed by comparing prognostic errors. At lower aerosol loadings, the fused AOD products yielded low uncertainties, overcoming large uncertainty of individual AOD products. The MLE AOD uncertainty increased sharply with aerosol loading; DNN AOD did not display such a behavior. Prognostic error analysis revealed that DNN-KO yielded the best performance, with lower uncertainty. A case of long-range aerosol transport was chosen for diurnal monitoring. MLE fusion, accounting for retrieval uncertainty from each aerosol algorithm, improved the hourly AOD distribution when compared with AERONET AOD. DNN AOD tracked AERONET AOD closely, yielding AOD estimates that were more closely aligned with AERONET values. The performance of aerosol data fusion can be improved with more dataset in the future study. For the MLE fusion, more sample leads to better representativeness of uncertainty weight. On the other hand, more dataset leads to better train performance of the DNN model. Moreover, DNN model in the future study will include more variables to predict optimal AOD. In April 2023, the US National Aeronautics and Space Administration launched the next series of global geostationary environmental

16

510 constellation instruments, TEMPO; the European Space Agency launched FCI in December 2022 and is planning to launch Sentinel-4 in 2025; and the NOAA GEOstationary eXtended Observations (GeoXO) satellite system is planned to form a constellation of geostationary satellite instruments. The application of aerosol fusion described here to these geostationary satellite projects may enable global production of high-quality aerosol data.

515 *Code availability.* The statistical and DNN-based aerosol fusion codes are available on request.

Data availability. The statistical and DNN-based aerosol fusion data are available on request.

Author Contributions. MK, HL, SG and JK designed the experiment. MK carried out the data processing. SL and YC provided
520 support with the data. MK wrote the manuscript, with contributions from all co-authors. JK reviewed and edited the article. JK provided support and supervision. All authors analyzed the measurement data and took part in manuscript preparation.

Competing Interests. The contact author has declared that none of the authors have any competing interests.

References

Ahn, C., Torres, O., and Jethva, H.: Assessment of OMI near-UV aerosol optical depth over land, J. Geophys Res-Atmos.,
535 119, 2457–2473, https//:doi.org/10.1002/2013jd020188, 2014.

Box, G. E. P. and Cox, D. R.: An Analysis of Transformations Revisited, Rebutted, J. Am Stat. Assoc., 77, 209–210, https//:doi.org/10.2307/2287791, 1982.

540   Cho, Y., Kim, J., Go, S., Kim, M., Lee, S., Kim, M., Chong, H., Lee, W. J., Lee, D. W., Torres, O., and Park, S. S.: First Atmospheric Aerosol Monitoring Results from Geostationary Environment Monitoring Spectrometer (GEMS) over Asia, Atmos. Meas. Tech. Disc., https://doi.org/10.5194/amt-2023-221, 2023.

Choi, J. K., Park, M. S., Han, K. S., Kim, H. C., and Im, J.: One Year of GOCI-II Launch Present and Future, Korean J. Remote
545   Sens., 37, 1229–1234, https//:doi.org/10.7780/kjrs.2021.37.5.2.1, 2021.

Choi, M., Kim, J., Lee, J., Kim, M., Park, Y. J., Holben, B., Eck, T. F., Li, Z. Q., and Song, C. H.: GOCI Yonsei aerosol retrieval version 2 products: an improved algorithm and error analysis with uncertainty estimation from 5-year validation over East Asia, Atmos. Meas. Tech., 11, 385–408, https//:doi.org/10.5194/amt-11-385-2018, 2018.
550
Choi, M., Kim, J., Lee, J., Kim, M., Park, Y. J., Jeong, U., Kim, W., Hong, H., Holben, B., Eck, T. F., Song, C. H., Lim, J. H., and Song, C. K.: GOCI Yonsei Aerosol Retrieval (YAER) algorithm and validation during the DRAGON-NE Asia 2012 campaign, Atmos. Meas. Tech., 9, 1377–1398, https//:doi.org/10.5194/amt-9-1377-2016, 2016.

555   Eck, T. F., Holben, B. N., Reid, J. S., Dubovik, O., Smirnov, A., O'Neill, N. T., Slutsker, I., and Kinne, S.: Wavelength dependence of the optical depth of biomass burning, urban, and desert aerosols, J. Geophys. Res-Atmos., 104, 31333–31349, https//:doi.org/10.1029/1999jd900923, 1999.

Giles, D. M., Sinyuk, A., Sorokin, M. G., Schafer, J. S., Smirnov, A., Slutsker, I., Eck, T. F., Holben, B. N., Lewis, J. R.,
560   Campbell, J. R., Welton, E. J., Korkin, S. V., and Lyapustin, A. I.: Advancements in the Aerosol Robotic Network (AERONET) Version 3 database - automated near-real-time quality control algorithm with improved cloud screening for Sun photometer aerosol optical depth (AOD) measurements, Atmos. Meas. Tech., 12, 169–209, https//:doi.org/10.5194/amt-12-169-2019, 2019.

565   Go, S., Lyapustin, A., Schuster, G. L., Choi, M., Ginoux, P., Chin, M. A., Kalashnikova, O., Dubovik, O., Kim, J., da Silva, A., Holben, B., and Reid, J. S.: Inferring iron-oxide species content in atmospheric mineral dust from DSCOVR EPIC observations, Atmos. Chem. Phys., 22, 1395–1423, https//:doi.org/10.5194/acp-22-1395-2022, 2022.

Gupta, P., Patadia, F., and Christopher, S. A.: Multisensor data product fusion for aerosol research, IEEE T Geosci. Remote,
570   46, 1407–1415, https//:doi.org/10.1109/Tgrs.2008.916087, 2008.

18

Holben, B. N., Eck, T. F., Slutsker, I., Tanre, D., Buis, J. P., Setzer, A., Vermote, E., Reagan, J. A., Kaufman, Y. J., Nakajima, T., Lavenu, F., Jankowiak, I., and Smirnov, A.: AERONET - A federated instrument network and data archive for aerosol characterization, Remote Sens. Environ., 66, 1–16, https//:doi.org/10.1016/S0034-4257(98)00031-5, 1998.

575

Hsu, N. C., Tsay, S. C., King, M. D., and Herman, J. R.: Deep blue retrievals of Asian aerosol properties during ACE-Asia, IEEE T Geosci. Remote Sens., 44, 3180–3195, https//:doi.org/10.1109/Tgrs.2006.879540, 2006.

Hsu, N. C., Jeong, M. J., Bettenhausen, C., Sayer, A. M., Hansell, R., Seftor, C. S., Huang, J., and Tsay, S. C.: Enhanced Deep
580 Blue aerosol retrieval algorithm: The second generation, J. Geophys.. Res-Atmos, 118, 9296–9315, https//:doi.org/10.1002/jgrd.50712, 2013.

Jethva, H., Torres, O., and Ahn, C.: A 12-year long global record of optical depth of absorbing aerosols above the clouds derived from the OMI/OMACA algorithm, Atmos. Meas. Tech., 11, 5837–5864, https//:doi.org/10.5194/amt-11-5837-2018,
585 2018.

Kahn, R., Banerjee, P., and McDonald, D.: Sensitivity of multiangle imaging to natural mixtures of aerosols over ocean, J. Geophys. Res-Atmos., 106, 18219–18238, https//:doi.org/10.1029/2000jd900497, 2001.

590 Ji, D. B., Shi, J. C., Letu, H., Wang, T. X., and Zhao, T. J.: Atmospheric Effect Analysis and Correction of the Microwave Vegetation Index, Remote Sens.-Basel, 9, ARTN 606 https//:doi.org/10.3390/rs9060606, 2017.

Kaufman, Y. J., Fraser, R. S., and Ferrare, R. A.: Satellite Measurements of Large-Scale Air-Pollution - Methods, J. Geophys. Res-Atmos., 95, 9895–9909, https//:doi.org/10.1029/JD095iD07p09895, 1990.

595

Kaufman, Y. J., Tanre, D., Remer, L. A., Vermote, E. F., Chu, A., and Holben, B. N.: Operational remote sensing of tropospheric aerosol over land from EOS moderate resolution imaging spectroradiometer, J. Geophys. Res-Atmos., 102, 17051–17067, https//:doi.org/10.1029/96jd03988, 1997.

600 Kim, D., Gu, M., Oh, T. H., Kim, E. K., and Yang, H. J.: Introduction of the Advanced Meteorological Imager of Geo-Kompsat-2a: In-Orbit Tests and Performance Validation, Remote Sens-Basel, 13, ARTN https//:doi.org/130310.3390/rs13071303, 2021.

19

Kim, M., Kim, J., Torres, O., Ahn, C., Kim, W., Jeong, U., Go, S., Liu, X., Moon, K. J., and Kim, D. R.: Optimal Estimation-Based Algorithm to Retrieve Aerosol Optical Properties for GEMS Measurements over Asia, Remote Sens.-Basel, 10, ARTN https://:doi.org/16210.3390/rs10020162, 2018.

Kim, M., Kim, J., Wong, M. S., Yoon, J., Lee, J., Wu, D., Chan, P. W., Nichol, J. E., Chung, C. Y., and Ou, M. L.: Improvement of aerosol optical depth retrieval over Hong Kong from a geostationary meteorological satellite using critical reflectance with background optical depth correction, Remote Sens. Environ., 142, 176–187, https://:doi.org/10.1016/j.rse.2013.12.003, 2014.

Kim, M., Kim, J., Jeong, U., Kim, W., Hong, H., Holben, B., Eck, T. F., Lim, J. H., Song, C. K., Lee, S., and Chung, C. Y.: Aerosol optical properties derived from the DRAGON-NE Asia campaign, and implications for a single-channel algorithm to retrieve aerosol optical depth in spring from Meteorological Imager (MI) on-board the Communication, Ocean, and Meteorological Satellite (COMS), Atmos. Chem. Phys., 16, 1789–1808, https://:doi.org/10.5194/acp-16-1789-2016, 2016.

Kim, M., Kim, S. H., Kim, W. V., Lee, Y. G., Kim, J., and Kafatos, M. C.: Assessment of Aerosol optical depth under background and polluted conditions using AERONET and VIIRS datasets, Atmos Environ, 245, ARTN 117994 https://:doi.org/10.1016/j.atmosenv.2020.117994, 2021.

Kim, M., Kim, J., Lim, H., Lee, S., Cho, Y., Chan, P. W.: Implementation of the Yonsei Aerosol retrieval algorithm in the GK-2A/AMI and FY-4A/AGRI remote-sensing systems. AIP Conf. Proc., 2988, 050002. https://doi.org/10.1063/5.0183243, 2024.

Kim, J., Jeong, U., Ahn, M. H., Kim, J. H., Park, R. J., Lee, H., Song, C. H., Choi, Y. S., Lee, K. H., Yoo, J. M., Jeong, M. J., Park, S. K., Lee, K. M., Song, C. K., Kim, S. W., Kim, Y. J., Kim, S. W., Kim, M., Go, S., Liu, X., Chance, K., Chan Miller, C., Al-Saadi, J., Veihelmann, B., Bhartia, P. K., Torres, O., Abad, G. G., Haffner, D. P., Ko, D. H., Lee, S. H., Woo, J. H., Chong, H., Park, S. S., Nicks, D., Choi, W. J., Moon, K. J., Cho, A., Yoon, J., Kim, S. K., Hong, H., Lee, K., Lee, H., Lee, S., Choi, M., Veefkind, P., Levelt, P. F., Edwards, D. P., Kang, M., Eo, M., Bak, J., Baek, K., Kwon, H. A., Yang, J., Park, J., Han, K. M., Kim, B. R., Shin, H. W., Choi, H., Lee, E., Chong, J., Cha, Y., Koo, J. H., Irie, H., Hayashida, S., Kasai, Y., Kanaya, Y., Liu, C., Lin, J., Crawford, J. H., Carmichael, G. R., Newchurch, M. J., Lefer, B. L., Herman, J. R., Swap, R. J., Lau, A. K. H., Kurosu, T. P., Jaross, G., Ahlers, B., Dobber, M., McElroy, C. T., and Choi, Y.: New Era of Air Quality Monitoring from Space: Geostationary Environment Monitoring Spectrometer (GEMS), B. Am. Meteorol. Soc., 101, E1–E22, https://:doi.org/10.1175/Bams-D-18-0013.1, 2020.

King, M. D., Kaufman, Y. J., Tanre, D., and Nakajima, T.: Remote sensing of tropospheric aerosols from space: Past, present, and future, B. Am. Meteorol. Soc., 80, 2229–2259, https://:doi.org/10.1175/1520-0477(1999)080<2229:Rsotaf>2.0.Co;2, 1999.

20

Lee, J., Kim, J., Song, C. H., Kim, S. B., Chun, Y., Sohn, B. J., and Holben, B. N.: Characteristics of aerosol types from
640   AERONET sunphotometer measurements, Atmos. Environ., 44, 3110–3117, https//:doi.org/10.1016/j.atmosenv.2010.05.035,
2010a.

Lee, J., Kim, J., Song, C. H., Ryu, J. H., Ahn, Y. H., and Song, C. K.: Algorithm for retrieval of aerosol optical properties over
the   ocean   from   the   Geostationary   Ocean   Color   Imager,   Remote   Sens.   Environ.,   114,   1077–1088,
645   https//:doi.org/10.1016/j.rse.2009.12.021, 2010b.

Lee, S., Kim, J., Choi, M., Hong, J., Lim, H., Eck, T. F., Holben, B. N., Ahn, J. Y., Kim, J., and Koo, J. H.: Analysis of long-
range transboundary transport (LRTT) effect on Korean aerosol pollution during the KORUS-AQ campaign, Atmos. Environ.,
204, 53–67, https//:doi.org/10.1016/j.atmosenv.2019.02.020, 2019.
650

Lee, S., Choi, M., Kim, J., Park, Y.-J., Choi, J.-K., Lim, H., Lee, J., Kim, M., and Cho, Y.: Retrieval of aerosol optical
properties from GOCI-II observations: Continuation of long-term geostationary aerosol monitoring over East Asia, Sci. Total.
Environ., 903, ARTN 166504 https//:doi.org/10.1016/j.scitotenv.2023.166504, 2023.

655   Levy, R. C., Mattoo, S., Munchak, L. A., Remer, L. A., Sayer, A. M., Patadia, F., and Hsu, N. C.: The Collection 6 MODIS
aerosol products over land and ocean, Atmos. Meas. Tech, 6, 2989–3034, https//:doi.org/10.5194/amt-6-2989-2013, 2013.

Lim, H., Choi, M., Kim, M., Kim, J., Go, S., and Lee, S.: Intercomparing the Aerosol Optical Depth Using the Geostationary
Satellite Sensors (AHI, GOCI and MI) from Yonsei AErosol Retrieval (YAER) Algorithm, J. Kor. Earth Sci. Soc., 39, 119–
660   130, https//:doi.org/10.5467/Jkess.2018.39.2.119, 2018.

Li, L., Jamieson, K., Rostamizadeh, A., Gonina, E., Hardt, M., Recht, B., and Talwalkar, A.: A System for Massively Parallel
Hyperparameter Tuning, Proceedings of the 3rd MLSys Conference, Austin, TX, USA, 2020.

665   Lim, H., Go, S., Kim, J., Choi, M., Lee, S., Song, C. K., and Kasai, Y.: Integration of GOCI and AHI Yonsei aerosol optical
depth products during the 2016 KORUS-AQ and 2018 EMeRGe campaigns, Atmos. Meas. Tech., 14, 4575–4592,
https//:doi.org/10.5194/amt-14-4575-2021, 2021.

Lin, T. H., Tsay, S. C., Lien, W. H., Lin, N. H., and Hsiao, T. C.: Spectral Derivatives of Optical Depth for Partitioning Aerosol
670   Type and Loading, Remote Sens.-Basel, 13, ARTN 1544 https//:doi.org/10.3390/rs13081544, 2021.

Lyapustin, A., Wang, Y. J., Korkin, S., and Huang, D.: MODIS Collection 6 MAIAC algorithm, Atmos. Meas. Tech., 11, 5741–5765, https//:doi.org/10.5194/amt-11-5741-2018, 2018.

675 Lyapustin, A., Martonchik, J., Wang, Y. J., Laszlo, I., and Korkin, S.: Multiangle implementation of atmospheric correction (MAIAC): 1. Radiative transfer basis and look-up tables, J. Geophys. Res-Atmos., 116, ARTN D03210 https//:doi.org/10.1029/2010jd014985, 2011a.

Lyapustin, A., Wang, Y., Laszlo, I., Kahn, R., Korkin, S., Remer, L., Levy, R., and Reid, J. S.: Multiangle implementation of 680 atmospheric correction (MAIAC): 2. Aerosol algorithm, J. Geophys.. Res-Atmos, 116, ARTN D03211 https//:doi.org/10.1029/2010jd014986, 2011b.

Lyapustin, A. I., Wang, Y. J., Laszlo, I., Hilker, T., Hall, F. G., Sellers, P. J., Tucker, C. J., and Korkin, S. V.: Multi-angle implementation of atmospheric correction for MODIS (MAIAC): 3. Atmospheric correction, Remote Sens. Environ., 127, 685 385–393, https//:doi.org/10.1016/j.rse.2012.09.002, 2012.

Lyapustin, A. I., Go, S., Korkin, S., Wang, Y., Torres, O., Jethva, H., and Marshak, A.: Retrievals of Aerosol Optical Depth and Spectral Absorption from DSCOVR EPIC, Front. Remote Sens., 2:645794, https//:doi.org/10.3389/frsen.2021.645794, 2021.

690

Park, S. S., Kim, S. -W., Song, C. -K., Park, J. -U., and Bae, K.: Spatio-Temporal Variability of Aerosol Optical Depth, Total Ozone and NO2 Over East Asia: Strategy for the Validation to the GEMS Scientific Products, Remote Sens., 12(14), 2020.

Remer, L. A., Kaufman, Y. J., Tanre, D., Mattoo, S., Chu, D. A., Martins, J. V., Li, R. R., Ichoku, C., Levy, R. C., Kleidman, 695 R. G., Eck, T. F., Vermote, E., and Holben, B. N.: The MODIS aerosol algorithm, products, and validation, J. Atmos Sci., 62, 947–973, https//:doi.org/10.1175/Jas3385.1, 2005.

Roskovensky, J. K. and Liou, K. N.: Detection of thin cirrus using a combination of 1.38-mu m reflectance and window brightness temperature difference, J. Geophys Res-Atmos., 108, ARTN 4570 https//:doi.org/10.1029/2002jd003346, 2003. 700 Sakia, R. M.: The Box-Cox Transformation Technique - a Review, J. Roy. Stat Soc. D-Sta, 41, 169–178, https//:doi.org/10.2307/2348250, 1992.

Sayer, A. M., Hsu, N. C., Bettenhausen, C., and Jeong, M. J.: Validation and uncertainty estimates for MODIS Collection 6 "Deep Blue" aerosol data, J. Geophys. Res-Atmos., 118, 7864–7872, https//:doi.org/10.1002/jgrd.50600, 2013.

705

서식 지정함: 영어(영국)

Sayer, A. M., Govaerts, Y., Kolmonen, P., Lipponen, A., Luffarelli, M., Mielonen, T., Patadia, F., Popp, T., Povey, A. C., Stebel, K., and Witek, M. L.: A review and framework for the evaluation of pixel-level uncertainty estimates in satellite aerosol remote sensing, Atmos. Meas. Tech., 13, 373–404, https//:doi.org/10.5194/amt-13-373-2020, 2020.

710   Tang, Q. X., Bo, Y. C., and Zhu, Y. X.: Spatiotemporal fusion of multiple-satellite aerosol optical depth (AOD) products using Bayesian maximum entropy method, J.. Geophys Res-Atmos., 121, 4034–4048, https//:doi.org/10.1002/2015jd024571, 2016.

Torres, O., Jethva, H., and Bhartia, P. K.: Retrieval of Aerosol Optical Depth above Clouds from OMI Observations: Sensitivity Analysis and Case Studies, J. Atmos. Sci., 69, 1037–1053, https//:doi.org/10.1175/Jas-D-11-0130.1, 2012.

715

Torres, O., Bhartia, P. K., Herman, J. R., Ahmad, Z., and Gleason, J.: Derivation of aerosol properties from satellite measurements of backscattered ultraviolet radiation: Theoretical basis, J. Geophys. Res-Atmos., 103, 17099–17110, https//:doi.org/ 10.1029/98jd00900, 1998.

720   Torres, O., Jethva, H., Ahn, C., Jaross, G., and Loyola, D. G.: TROPOMI aerosol products: evaluation and observations of synoptic-scale carbonaceous aerosol plumes during 2018-2020, Atmos. Meas. Tech., 13, 6789–6806, https//:doi.org/10.5194/amt-13-6789-2020, 2020.

Torres, O., Bhartia, P. K., Herman, J. R., Sinyuk, A., Ginoux, P., and Holben, B.: A long-term record of aerosol optical depth
725   from TOMS observations and comparison to AERONET measurements, J. Atmos. Sci., 59, 398–413, https//:doi.org/10.1175/1520-0469(2002)059<0398:Altroa>2.0.Co;2, 2002.

Tuckey, J. W.: On the Comparative Anatomy of Transformations, The Annals of Math. Stat., 28, 3, 602–632, 1957.

730   von Hoyningen-Huene, W., Yoon, J., Vountas, M., Istomina, L. G., Rohen, G., Dinter, T., Kokhanovsky, A. A., and Burrows, J. P.: Retrieval of spectral aerosol optical thickness over land using ocean color sensors MERIS and SeaWiFS, Atmos. Meas. Tech., 4, 151–171, https//:doi.org/10.5194/amt-4-151-2011, 2011.

Wei, J., Li, Z. Q., Sun, L., Peng, Y. R., and Wang, L. C.: Improved merge schemes for MODIS Collection 6.1 Dark Target
735   and Deep Blue combined aerosol products, Atmos. Environ., 202, 315–327, https//:doi.org/10.1016/j.atmosenv.2019.01.016, 2019.

Xie, Y. Q., Xue, Y., Che, Y. H., Guang, J., Mei, L. L., Voorhis, D., Fan, C., She, L., and Xu, H.: Ensemble of ESA/AATSR Aerosol Optical Depth Products Based on the Likelihood Estimate Method With Uncertainties, IEEE T Geosci. Remote, 56, 740 997–1007, https//:doi.org/10.1109/Tgrs.2017.2757910, 2018.

Xu, H., Guang, J., Xue, Y., de Leeuw, G., Che, Y. H., Guo, J. P., He, X. W., and Wang, T. K.: A consistent aerosol optical depth (AOD) dataset over mainland China by integration of several AOD products, Atmos. Environ., 114, 48–56, https//:doi.org/10.1016/j.atmosenv.2015.05.023, 2015.
745

Xue, Y., Xu, H., Guang, J., Mei, L., Guo, J., Li, C., Mikusauskas, R., and He, X.: Observation of an agricultural biomass burning in central and east China using merged aerosol optical depth data from multiple satellite missions, Int. J. Remote Sens., 35, 5971–5983, https//:doi.org/10.1080/2150704x.2014.943321, 2014.

750 Yin, S.: Biomass burning spatiotemporal variations over South and Southeast Asia, Environ. Int., 145, ARTN 106153 https//:doi.org/10.1016/j.envint.2020.106153, 2020.
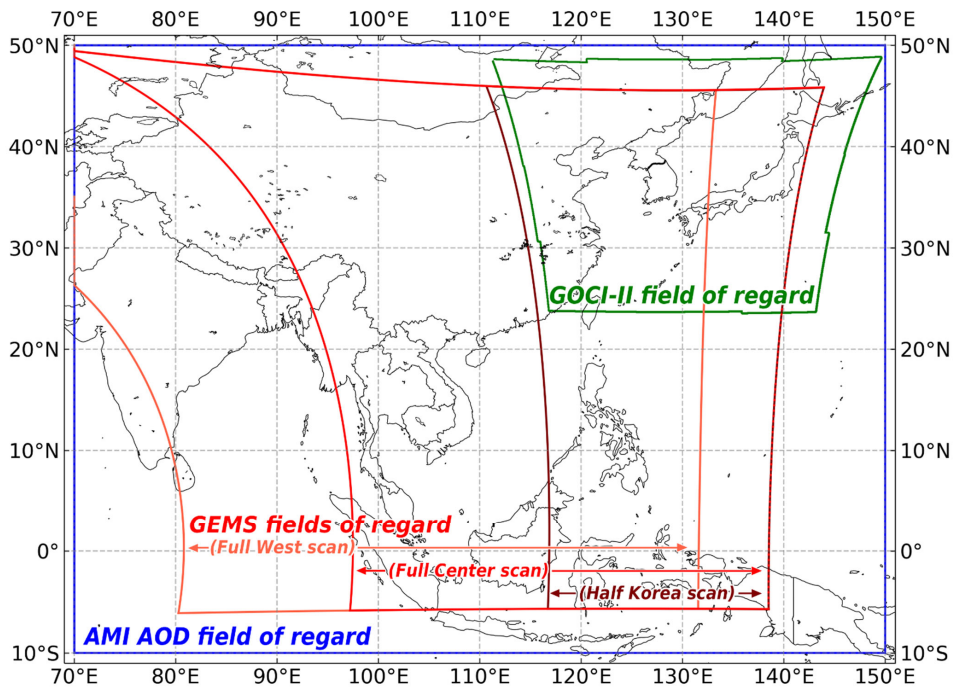
Figure 1. Fields of regard for GEMS, AMI, and GOCI-II. AMI AOD were retrieved only within the 70°E–150°E, 10°S–50°N area to match the GEMS field of regard.
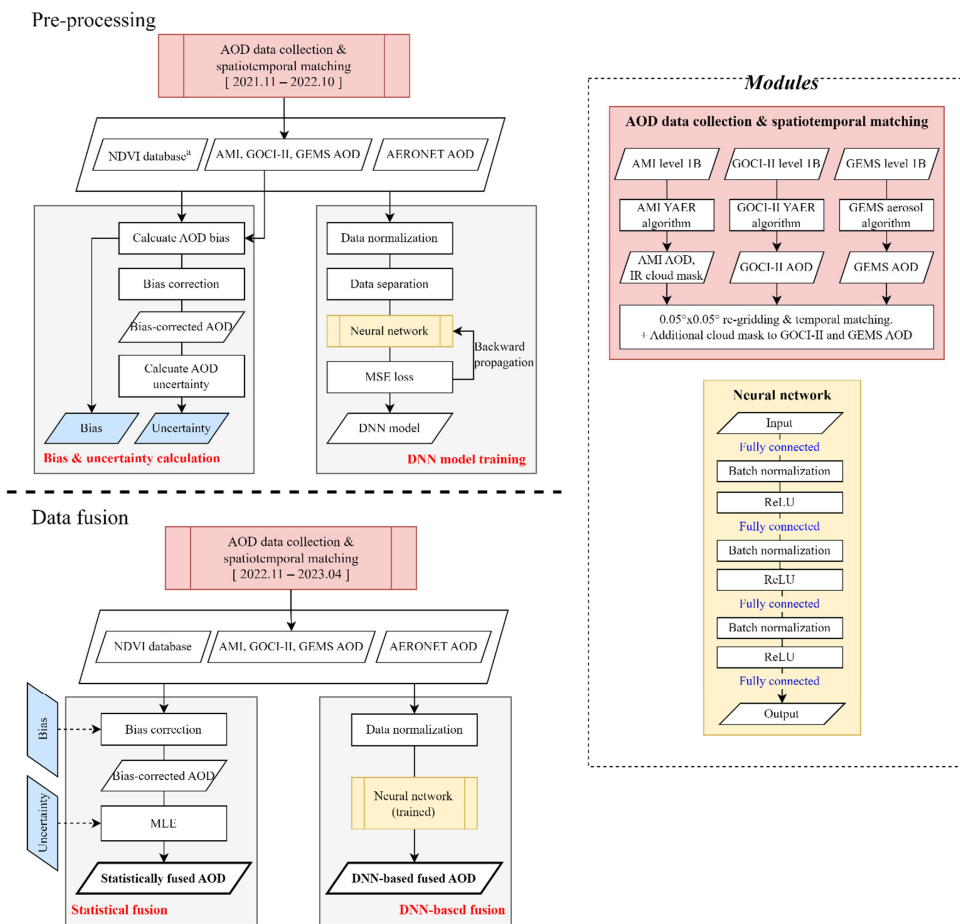
Figure 2. Flowchart of the fusion algorithm. Red- and yellow-colored boxes represent commonly used modules for both preprocessing and data fusion procedures. The Normalized Differential Vegetation Index (NDVI) database[a] was generated using AMI Minimum Reflectance Method (MRM) surface reflectance in green, red, and Near-Infrared (NIR) channels.
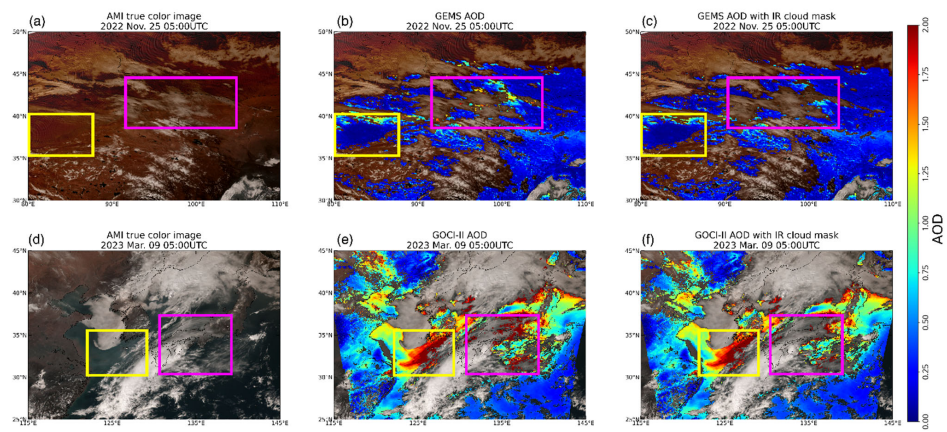
Figure 3. Examples of additional Infrared (IR) cloud masking for GEMS and GOCI-II AOD. (a–c) A case of GEMS AOD on 25 November 2022; (d–f) A case of GOCI-II AOD on 09 March 2023. Each column shows an AMI true color image, original AOD, and AOD with additional cloud mask of corresponding cases. Yellow boxes correspond to cloud-free zones; magenta boxes correspond to areas in which GEMS or GOCI-II misidentified cloud pixels.

765

27
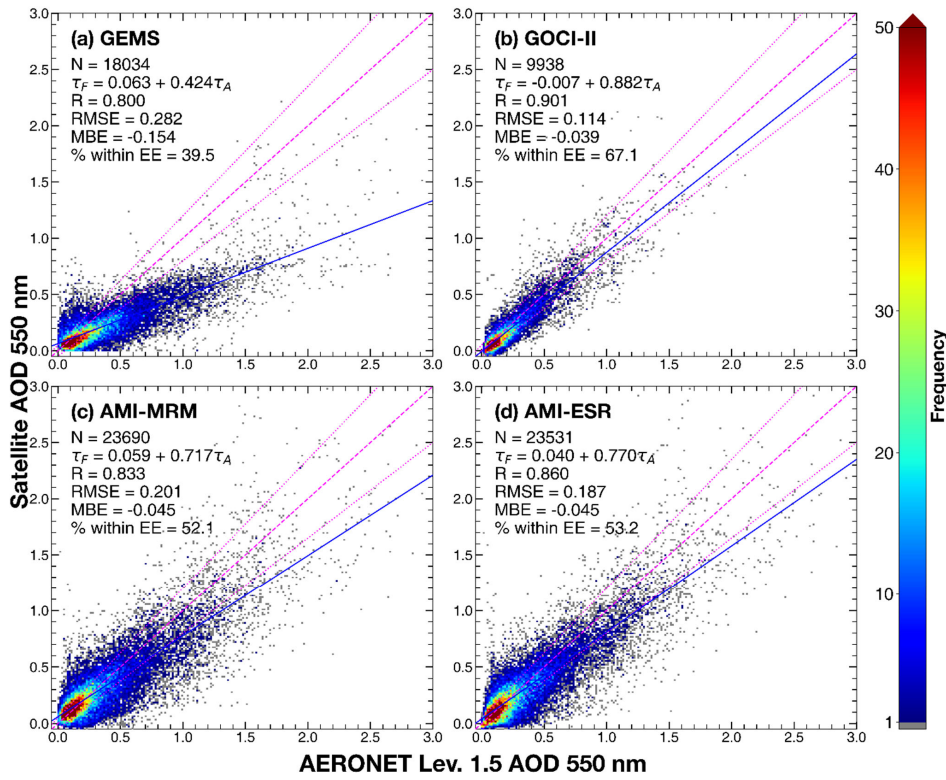
Figure 4. 2-dimensional histograms of AERONET AOD vs. GEMS (a), GOCI–II (b), AMI–MRM (c), and AMI–ESR AOD (d) frequencies. The number of collocated points (N), linear regression equations, Pearson's correlation coefficient (R), root mean squared errors (RMSE), mean bias errors (MBE), and percentage within the expected error envelope (% within EE; EE: $\pm(0.05+0.15\ \tau_A)$) is shown. Dashed line and dotted lines indicate one-to-one line and expected error envelopes. Blue line indicates linear regression line of the satellite AOD and AERONET AOD
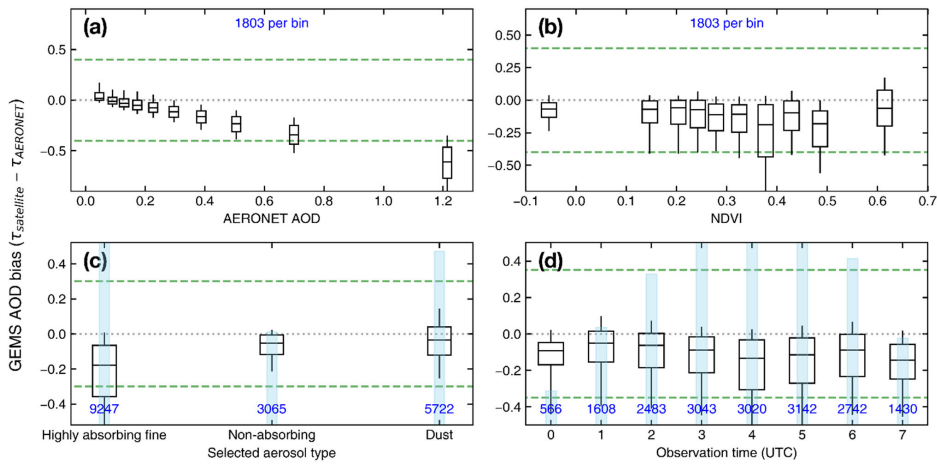
28

Figure 5. AOD bias of GEMS AOD relative to AERONET AOD (a), NDVI (b), selected aerosol type (c), and observation time (d). Whisker ends correspond to the 10th and 90th percentiles of the bin. Box ends correspond to the 25th and 75th percentiles. Horizontal lines in each box indicate bin median. Green dashed line indicates the y-axis range of GOCI-II AOD in corresponding panels. Numbers and bar plots in blue indicate the number of collocated AOD points in each box–whisker.
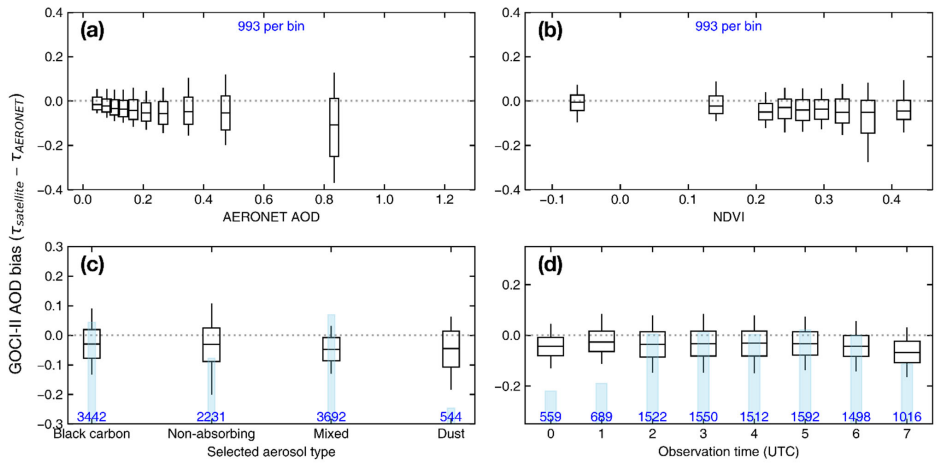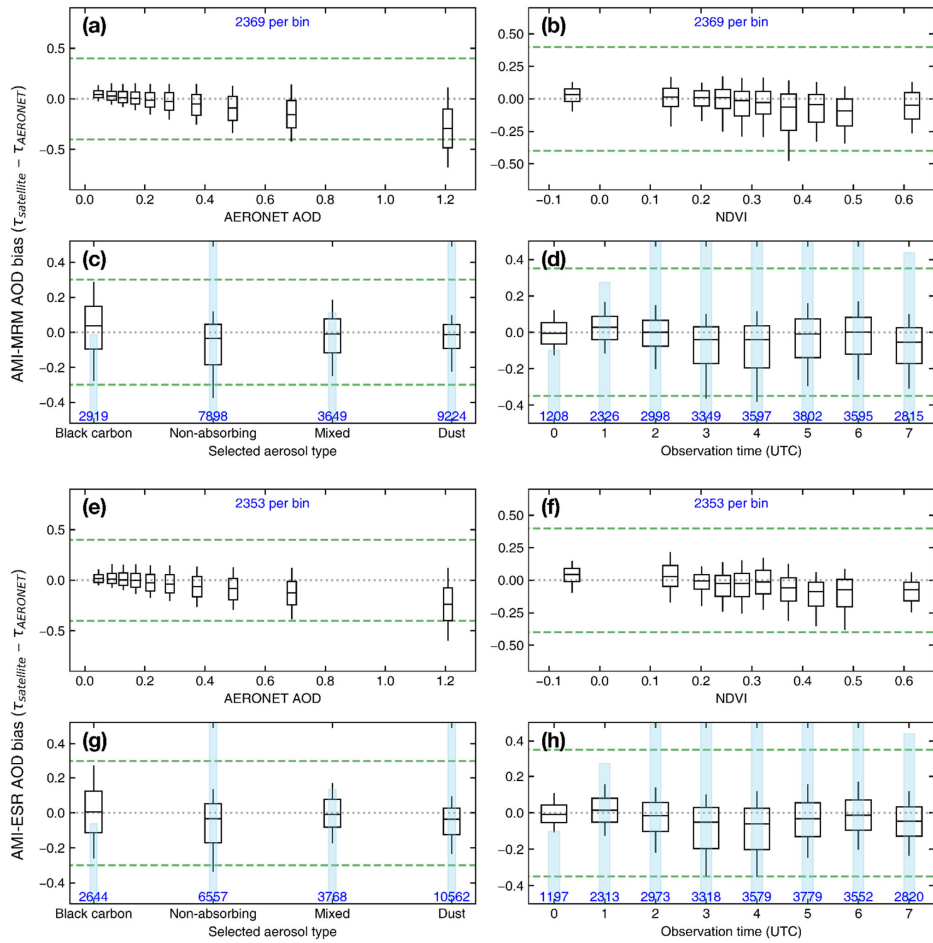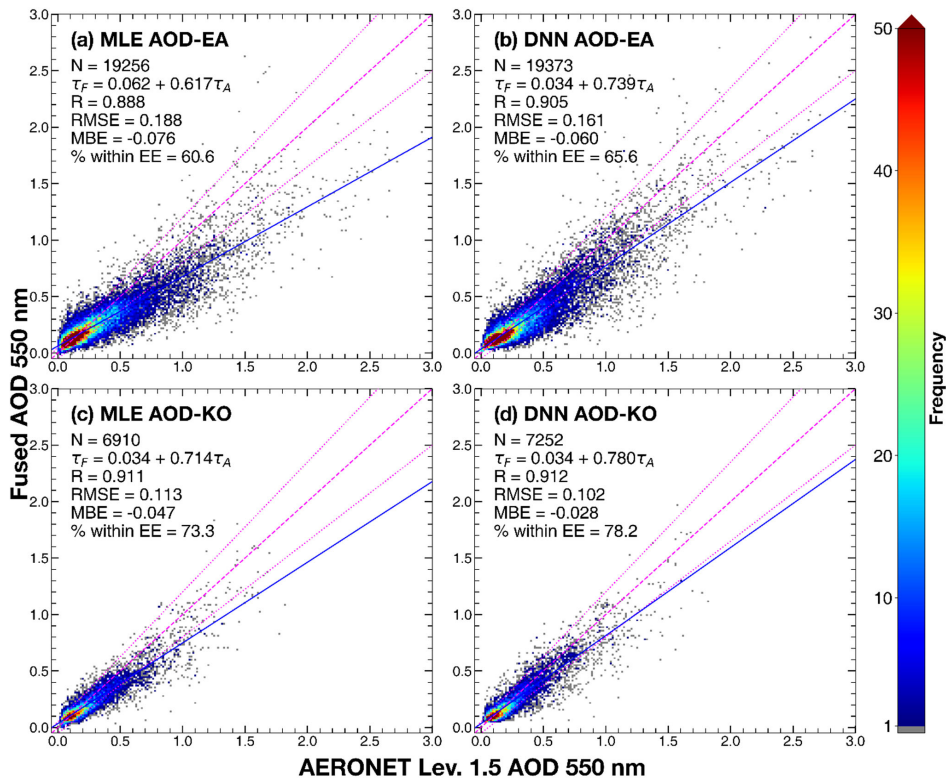
Figure 6. As for Fig. 5, but for GOCI-II AOD.

785   **Figure 7. As for Fig. 5, but for AMI–MRM and AMI–ESR AOD.**

Figure 8. As for Fig. 4, but for Maximum Likelihood Estimation (MLE) AOD-EA (a), Deep Neural Network (DNN) AOD-EA (b), MLE AOD-KO (c), and DNN AOD-KO (d).
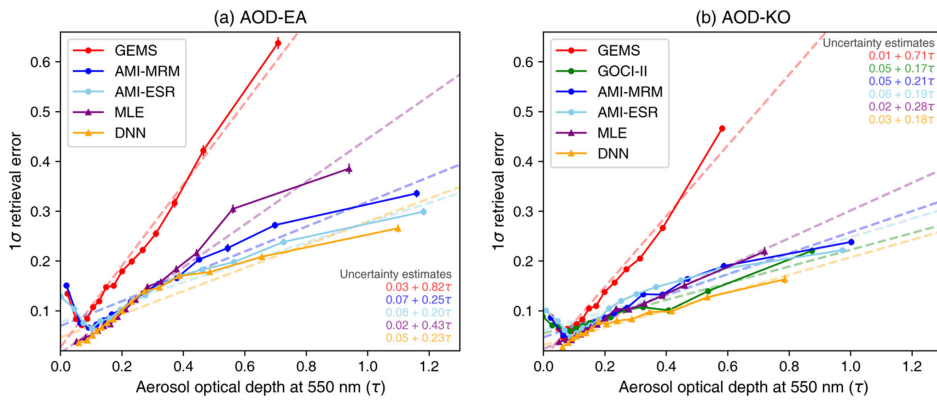
Figure 9. Changes in uncertainty of AOD products with increasing AOD. 68th percentile value of retrieval error is defined as 1σ retrieval error and plotted against AOD value. Vertical lines of each marker represent the difference of 67th and 69th percentiles, thus indicating the error of 1σ retrieval error. Dashed lines show linear regression (uncertainty estimates) of 1σ retrieval error.
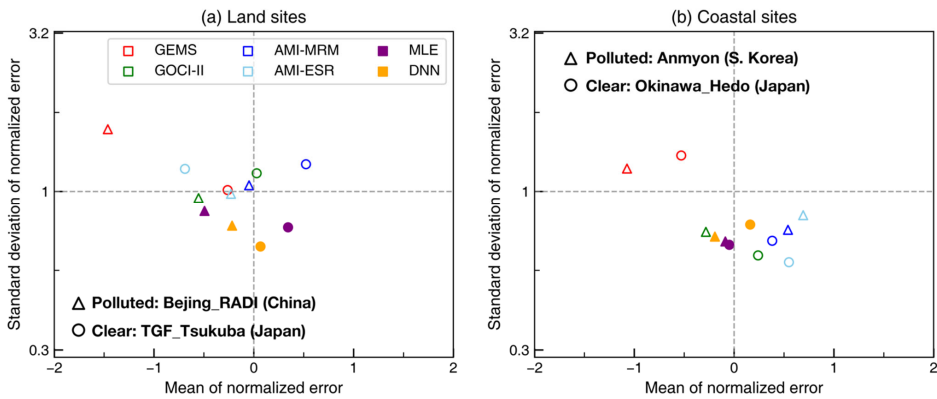
Figure 10. Mean and standard deviation of normalized error for each AOD product collocated at selected land (a) and coastal (b) AERONET sites. The Bejijing_RADI and TGF_Tsukuba sites were chosen to represent polluted atmosphere over land and ocean, respectively. The Anmyon and Okinawa_Hedo sites were chosen to represent clear atmosphere over land and ocean, respectively.
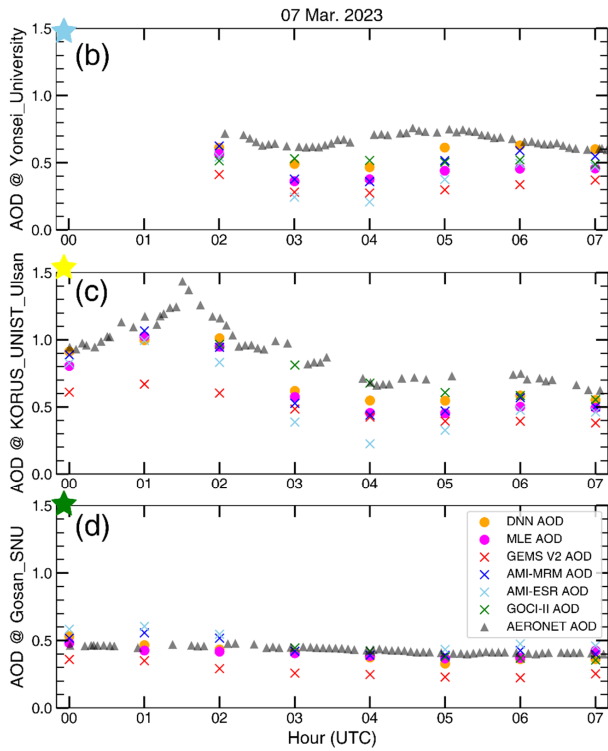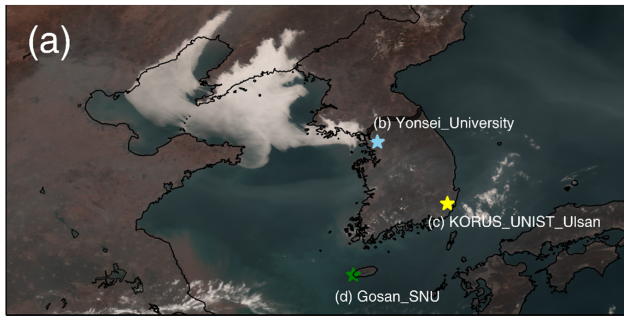
Figure 11. A case of aerosol transport over the Korean Peninsula on 07 March 2023. (a) AMI true color image at 04 UTC. (b)–(d) correspond to AERONET sites marked in (a). Gray triangles indicate AERONET AOD; original satellite AOD products are

805 **indicated by × symbols in different colors; fused AOD products around the Korean Peninsula (AOD-KO) are indicated by circles in different colors.**

Table 1: Specification of instruments in Geo Kompsate-2 (GK-2) mission.

| Satellite	GK-2A	GK-2B	
Payload	AMI	GOCI-II	GEMS
Channels	16	14	1,024
Spatial resolution of radiance	0.5 km (red), 1 km (VIS), 2 km (IR)	0.25 km	3.5 km × 7.7 km
Temporal resolution	10 min (full-disk scan)	1 h	1 h
Wavelength range	0.4–13 μm	375–860 nm	300–500 nm
FWHM	10–20 nm	10–20nm	0.6 nm
Launch	December 2018	February 2020	
Lifetime	10 years		
Location	128.2°		
Details of aerosol products			
Aerosol algorithm	AMI YAER algorithm (Kim et al., 2024)	GOCI-II YAER algorithm (Lee et al., 2023)	GEMS AERAOD retrieval algorithm (Cho et al., 2023)
Spatial resolution of aerosol product	6 km	2.5 km	3.5 km × 7.7 km
Land surface reflectance estimation	MRM & Estimation from SWIR channel	Minimum reflectance method (MRM)	
Ocean surface reflectance estimation	Cox & Munk method (Cox and Munk, 1954)		MRM
Inversion channels	VIS-NIR 4 bands	UV-NIR 12 bands	UV-VIS 6 spectrally binned bands
Algorithm version	Research algorithm	Ver. 1.1	Ver. 2.0

34

Table 2 The AERONET site information used in this study. All sites had valid collocation at level 1.5 with spaceborne AOD product from November, 2022 to April, 2023. Site names with asterisk (*) refers to sites where level 2.0 data from November, 2021 to October, 2022 are used for pre-processing.

#	Site name	Longitude (°E)	Latitude (°N)	Elevation (m)	#	Site name			
					46	*Gwangju_GIST	126.843	35.228	52
1	AOE_Baotou	109.629	40.852	1314	47	*Hankuk_UFS	127.266	37.339	167
2	*ARIAKE_TOWER	130.272	33.104	15	48	*Hokkaido_University	141.341	43.075	59
3	*Amity_Univ_Gurgaon	76.916	28.317	285	49	*Hong_Kong_PolyU	114.18	22.303	30
4	*Anmyon	126.33	36.539	47	50	*Hong_Kong_Sheung	114.117	22.483	40
5	*BMKG_GAW_PALU	120.183	-1.65	1370	51	*IIT_Delhi	77.193	28.545	15
6	Baengnyeong	124.63	37.966	136	52	*Jaipur	75.806	26.906	450
7	*Bangkok	100.518	13.749	57	53	*Jambi	103.642	-1.632	30
8	Beijing-CAMS	116.317	39.933	106	54	*KORUS_UNIST_Ulsan	129.19	35.582	106
9	Beijing	116.381	39.977	92	55	*Kanpur	80.232	26.513	123
10	Beijing_PKU	116.31	39.992	53	56	*Kaohsiung	120.292	22.676	15
11	Beijing_RADI	116.379	40.005	59	57	*Kemigawa_Offshore	140.023	35.611	8
12	*Bhola	90.756	22.227	7	58	*Lahore	74.264	31.48	209
13	Bidur	85.14	27.895	576	59	*Lulin	120.874	23.469	2868
14	*Bukit_Kototabang	100.318	-0.202	864	60	*Makassar	119.572	-4.998	16
15	*Cape_Fuguei_Station	121.538	25.297	40	61	Mandalay_MTU	96.186	21.973	104
16	*Chachoengsao	101.45	13.5	60	62	*Manila_Observatory	121.078	14.635	63
17	Chen-Kung_Univ	120.205	22.993	50	63	*NAM_CO	90.962	30.773	4746
18	Chiang_Dao	98.961	19.455	450	64	*ND_Marbel_Univ	124.843	6.496	70
19	*Chiang_Mai_Met_Sta	98.972	18.771	312	65	*Niigata	138.942	37.846	10
20	*Chiba_University	140.104	35.625	60	66	*Nong_Khai	102.717	17.877	175
21	*DRAGON_Hakuba	137.864	36.701	703	67	*Noto	137.137	37.334	200
22	*DRAGON_Iida	137.842	35.517	490	68	Okinawa_Hedo	128.249	26.867	60
23	*DRAGON_Ina	137.961	35.847	683	69	*Osaka	135.591	34.651	50
24	*DRAGON_Kofu	138.572	35.679	314	70	*Palangkaraya	113.946	-2.228	27
25	*DRAGON_Matsumoto	137.978	36.251	626	71	*Pokhara	83.975	28.187	800

35

26	*DRAGON_Minowa	137.981	35.915	713	72	*Pontianak	109.191	0.075	2
27	*DRAGON_Mt_Happo	137.798	36.697	1846	73	*QOMS_CAS	86.948	28.365	4276
28	*DRAGON_Mt_Haruna	138.878	36.475	1359	74	*Seoul_SNU	126.951	37.458	116
29	*DRAGON_Mt_Krigamine	138.168	36.098	1674	75	Shirahama	135.357	33.693	10
30	*DRAGON_Omachi	137.851	36.503	751	76	Silpakorn_Univ	100.041	13.819	72
31	*DRAGON_Suwa	138.109	36.046	766	77	*Singapore	103.78	1.298	30
32	*DRAGON_Takayama	137.304	36.253	1296	78	*Socheongcho	124.738	37.423	28
33	*Dalanzadgad	104.419	43.577	1470	79	Songkhla_Met_Sta	100.605	7.184	15
34	*Dhaka_University	90.398	23.728	34	80	*Sorong	131.268	-0.875	127
35	*Dibrugarh_Univ	94.897	27.451	119	81	*Sra_Kaeo	102.504	13.689	68
36	*Doi_Ang_Khang	99.045	19.932	1536	82	*TASA_Taiwan	121.001	24.784	99
37	*Dongsha_Island	116.729	20.699	5	83	*TGF_Tsukuba	140.096	36.114	25
38	Douliu	120.545	23.712	60	84	*Tai_Ping	114.362	10.376	4
39	*EPA-NCU	121.185	24.968	144	85	*Taipei_CWB	121.538	25.015	26
40	Erlin	120.41	23.925	16	86	*USM_Penang	100.302	5.358	51
41	*Fukue	128.682	32.752	80	87	Ubon_Ratchathani	104.871	15.246	120
42	*Fukuoka	130.475	33.524	30	88	*Ussuriysk	132.163	43.7	280
43	*Gandhi_College	84.128	25.871	60	89	*XiangHe	116.962	39.754	36
44	*Gangneung_WNU	128.867	37.771	60	90	*Xitun	120.617	24.162	91
45	*Gosan_NIMS_SNU	126.206	33.3	52	91	*Yonsei_University	126.935	37.564	97

Table 3: Cloud masking tests of AMI Yonsei AErosol Retrieval (YAER) algorithm.

Cloud detection test	Threshold	Surface type
BTD 9 max	<−28	Only over land
BTD 14 max	<−28	
Reflectance 1.3	>0.025	Over both land and ocean
BTD 15, 16	<10	
BTD 13, 16	≤11	

815

Table 4: Different cases of AOD availability in the fusion process and corresponding data fusion strategies.

	GEMS	AMI (MRM, ESR)	GOCI-II	MLE fusion	DNN fusion
AOD availability	○	○	○	Bias-corrected + MLE	Separate DNN model for each case
	○	○			
	○		○		
		○	○		
	○				
		○		Bias-corrected	
			○		

Table 5: Validation statistics of original AOD products and fused AOD products in -EA region. Validation period is from November 2022 to April 2023.

	Original AOD products			Fused AOD products	
	GEMS	AMI-MRM	AMI-ESR	MLE AOD	DNN AOD
R	0.800	0.834	0.860	0.888	0.905
RMSE	0.287	0.201	0.187	-0.188	0.161
MBE	-0.154	-0.045	-0.045	-0.076	-0.060
% within EE	39.5	52.1	53.3	60.6	65.6

Table 6: Validation statistics of original AOD products and fused AOD products in -KO region.

	Original AOD products	Fused AOD products

37

	GEMS	AMI-MRM	AMI-ESR	GOCI-II	MLE AOD	DNN AOD
R	0.807	0.878	0.867	0.901	0.911	0.912
RMSE	0.187	0.129	0.129	0.114	0.113	0.102
MBE	-0.086	0.017	-0.002	-0.038	-0.047	-0.028
% within EE	51.7	63.1	58.8	67.1	73.3	78.2